Article

A phosphate-sensing organelle regulates phosphate and tissue homeostasis

Chiwei Xu[1,8,11]✉, Jun Xu[1,9,11], Hong-Wen Tang[1,10], Maria Ericsson[2], Jui-Hsia Weng[3], Jonathan DiRusso[1], Yanhui Hu[1], Wenzhe Ma[4], John M. Asara[5,6] & Norbert Perrimon[1,7]✉

Inorganic phosphate (P_i) is one of the essential molecules for life. However, little is known about intracellular P_i metabolism and signalling in animal tissues[1]. Following the observation that chronic P_i starvation causes hyperproliferation in the digestive epithelium of *Drosophila melanogaster*, we determined that P_i starvation triggers the downregulation of the P_i transporter *PXo*. In line with P_i starvation, *PXo* deficiency caused midgut hyperproliferation. Interestingly, immunostaining and ultrastructural analyses showed that PXo specifically marks non-canonical multilamellar organelles (PXo bodies). Further, by P_i imaging with a Förster resonance energy transfer (FRET)-based P_i sensor[2], we found that PXo restricts cytosolic P_i levels. PXo bodies require PXo for biogenesis and undergo degradation following P_i starvation. Proteomic and lipidomic characterization of PXo bodies unveiled their distinct feature as an intracellular P_i reserve. Therefore, P_i starvation triggers *PXo* downregulation and PXo body degradation as a compensatory mechanism to increase cytosolic P_i. Finally, we identified connector of kinase to AP-1 (Cka), a component of the STRIPAK complex and JNK signalling[3], as the mediator of *PXo* knockdown- or P_i starvation-induced hyperproliferation. Altogether, our study uncovers PXo bodies as a critical regulator of cytosolic P_i levels and identifies a P_i-dependent PXo–Cka–JNK signalling cascade controlling tissue homeostasis.

Inorganic phosphate (P_i) is consumed by use in post-translational modifications and the synthesis of essential metabolites. Despite its universal importance for life, P_i metabolism has mostly been studied in bacteria, yeast and plants. In bacteria, P_i is stored in polyphosphate granules[4] whereas, in yeast and plant cells, P_i is mainly stored in vacuoles[5]. It has also been proposed that P_i-containing biomolecules such as polyphosphate (in bacteria and fungi)[6] and membrane phospholipids (in plants)[7] might serve as a P_i reserve. In animals, although much has been learned about the hormonal regulation of circulating P_i (ref. 8), little is known about intracellular P_i metabolism and signalling.

The epithelium of the adult *Drosophila* midgut is composed of large enterocytes, hormone-secretary enteroendocrine cells, *esg*+ progenitors including intestinal stem cells (ISCs) and postmitotic enteroblasts[9]. Enterocytes are the major cell type in the midgut and are a prominent site of nutrient absorption. ISCs and enteroblasts can adjust proliferation and differentiation activity and produce enterocytes or enteroendocrine cells in response to fluctuating environmental stimuli to meet the demands of tissue regeneration[10]. To evaluate how P_i levels impact midgut tissue homeostasis, we fed flies phosphonoformic acid (PFA), an inorganic pyrophosphate analogue and potent inhibitor of cellular P_i uptake[8]. A significant increase in midgut mitosis (indicated by staining for phosphorylated histone H3 (pH3)) was observed following chronic P_i starvation (Fig. 1a and Extended Data Fig. 1a,b). To verify our finding, we fed flies chemically defined food (CDF) and found that reducing dietary P_i to 10% of standard levels could also induce midgut mitosis (Fig. 1b and Extended Data Fig. 1c,d). Furthermore, we genetically recapitulated P_i starvation using knockdown of *MFS10* (encoding a P_i uptake transporter)[8] in enterocytes. In agreement with our experiments using PFA and CDF, we observed an increase in midgut proliferation following *MFS10* knockdown under normal conditions or with bleomycin-induced tissue damage (Fig. 1c; knockdown confirmed in Extended Data Fig. 1e). Contrary to the idea that P_i starvation might induce compensatory P_i uptake through MFS10, PFA feeding decreased midgut *MFS10* expression (Fig. 1d). Moreover, a cell loss assay for enterocytes labelled with histone 2B fused to red fluorescent protein (H2B–RFP) showed accelerated enterocyte turnover following P_i starvation (Fig. 1e and Extended Data Fig. 1f,g), suggesting that P_i starvation-induced ISC hyperproliferation is regenerative. However, whereas enterocyte apoptosis triggers regenerative ISC proliferation under tissue damage conditions[10], P_i starvation did not induce massive apoptosis in the midgut (Fig. 1f and Extended Data Fig. 1h–j). Collectively, these data raise the question of how the midgut can maintain

[1]Department of Genetics, Blavatnik Institute, Harvard Medical School, Boston, MA, USA. [2]Department of Cell Biology, Electron Microscopy Facility, Blavatnik Institute, Harvard Medical School, Boston, MA, USA. [3]Institute of Biological Chemistry, Academia Sinica, Taipei, Taiwan. [4]Department of Systems Biology, Harvard Medical School, Boston, MA, USA. [5]Department of Medicine, Blavatnik Institute, Harvard Medical School, Boston, MA, USA. [6]Department of Signal Transduction, Beth Israel Deaconess Medical Center, Boston, MA, USA. [7]Howard Hughes Medical Institute, Harvard Medical School, Boston, MA, USA. [8]Present address: Robin Chemers Neustein Laboratory of Mammalian Development and Cell Biology, The Rockefeller University, New York, NY, USA. [9]Present address: CAS Key Laboratory of Insect Developmental and Evolutionary Biology, CAS Center for Excellence in Molecular Plant Sciences, Chinese Academy of Sciences, Shanghai, China. [10]Present address: Program in Cancer and Stem Cell Biology, Duke–NUS Medical School, Singapore, Singapore. [11]These authors contributed equally: Chiwei Xu, Jun Xu. ✉e-mail: charlesxu.harvard@gmail.com; perrimon@receptor.med.harvard.edu
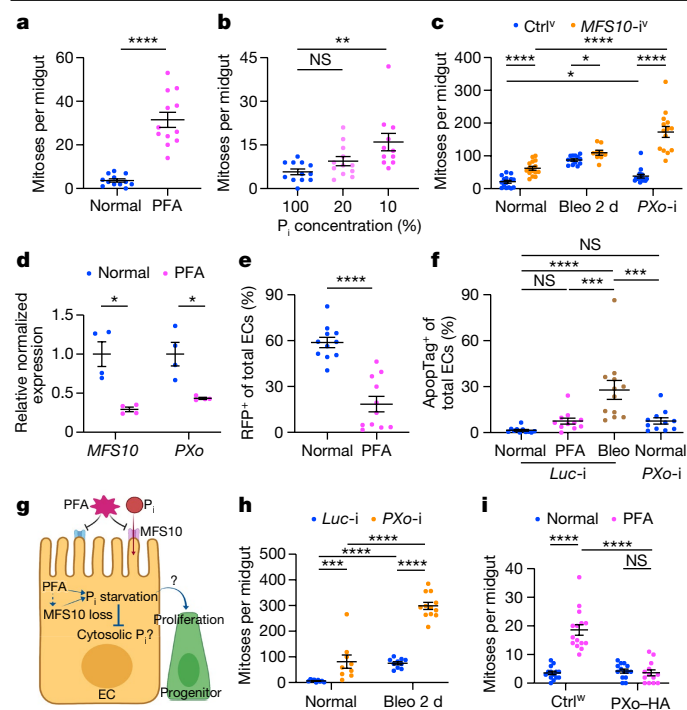
Fig. 1 | P_i deprivation or *PXo* deficiency induces midgut hyperproliferation. **a**, Mitosis of midguts from flies fed for 8 days with normal or PFA food. $n = 12$ per group. $P = 7.40 \times 10^{-7}$. **b**, Mitosis of midguts from flies fed for 9 days with CDF containing 100% ($n = 12$), 20% ($n = 12$; $P = 0.377$) or 10% ($n = 11$; $P = 1.74 \times 10^{-3}$) P_i. NS, not significant. **c**, Mitosis of midguts following *MFS10* (*MFS10*-i, with superscript label 'v' referring to VDRC reagents) or control knockdown in enterocytes under normal ($n = 15$ and 15), bleomycin feeding (Bleo) ($n = 9$ and 13) and *PXo* RNAi (*PXo*-i) ($n = 14$ and 15) conditions. P values from left to right: 3.65×10^{-6}, 0.0337, 0.0105, 1.81×10^{-7}, 6.45×10^{-8}. Ctrl, control. **d**, RT–qPCR of *MFS10* ($P = 0.0192$) and *PXo* (P1 primers; $P = 0.0323$) in midguts from flies fed for 6 days with normal or PFA food. $n = 4$ biological replicates per group. **e**, Percentage of H2B–RFP-marked enterocytes (ECs) after 9 days of normal or PFA feeding. $n = 11$ per group. $P = 5.67 \times 10^{-6}$. **f**, Percentage of ApopTag-positive enterocytes with expression of *Luc* (*Luc*-i) or *PXo* RNAi constructs for 7 days, fed normal food, PFA or for the last 2 days with bleomycin. $n = 11$ (*Luc*-i normal, PFA and *PXo*-i) and 12 (*Luc*-i bleomycin). P values from left to right: 0.763, 1.78×10^{-5}, 0.747, 2.76×10^{-4} and 7.37×10^{-4}. **g**, P_i starvation responses and questions for this study. Diagram created using BioRender.com. **h**, Mitosis of midguts from flies expressing *Luc* or *PXo* RNAi in enterocytes for 7 days, with or without 2 days of bleomycin. From left to right: $n = 9, 9, 10$ and 12; $P = 2.88 \times 10^{-4}$, 2.17×10^{-5}, 4.76×10^{-5} and 3.09×10^{-6}. **i**, Mitosis of midguts expressing *PXo-HA* in enterocytes for 8 days, fed normal or PFA food. Flies with the same genetic background were used as the control (with superscript 'w' referring to *w1118*). From left to right: $n = 14, 15, 14$ and 13; $P = 2.58 \times 10^{-8}$, 1.34×10^{-7} and 0.376. Data are shown as mean ± s.e.m. P values (NS ≥ 0.05, $*P < 0.05$, $**P < 0.01$, $***P < 1 \times 10^{-3}$, $****P < 1 \times 10^{-4}$) were obtained by two-tailed Mann–Whitney U test in **a,c,e,f,h,i**, two-tailed Welch's t-test in **d** or one-way ANOVA with Bonferroni's multiple-comparisons test in **b** and for comparison to *Luc*-i normal in **f**.

essential P_i levels and accelerate proliferation in response to restricted P_i uptake (Fig. 1g).

By examining transporters or putative P_i-sensing receptors among progenitor activity regulators identified in our previous in vivo RNA interference (RNAi) screen[11], we identified a candidate gene, *CG10483*, whose knockdown induces similar levels of midgut hyperproliferation as seen with P_i starvation. *CG10483*, which we renamed *PXo* (for P_i-sensitive XPR1 orthologue), is the orthologue of mammalian *XPR1* (xenotropic and polytropic retrovirus receptor 1) and encodes an eight-transmembrane-domain protein with a SYG1/Pho81/XPR1 (SPX) domain that senses P_i-derived inositol polyphosphate (InsPs)[12] and an EXS domain that is required for P_i transport[13]. Reverse transcription

with quantitative PCR (RT–qPCR) showed that *PXo* expression was downregulated in the midgut following P_i starvation (Fig. 1d). Expression of three different *PXo* RNAi constructs (target regions in Extended Data Fig. 2a; knockdown confirmed in Extended Data Fig. 2b) in either enterocytes or progenitors induced mitosis under both normal feeding and tissue damage conditions (Fig. 1h and Extended Data Fig. 1l–u). Like P_i starvation, *PXo* knockdown in enterocytes did not cause a significant increase in apoptosis (Fig. 1f and Extended Data Fig. 1k). Moreover, the anti-apoptotic factor p35 could not block midgut hyperproliferation when coexpressed with a *PXo* RNAi construct in either progenitors or enterocytes (Extended Data Fig. 1t,v). Lineage tracing of *esg*[+] progenitors with the EGT F/O system showed more active Pdm1^{+} enterocyte differentiation (Extended Data Fig. 2i–n) and no apoptosis (Extended Data Fig. 2o,p) under P_i starvation or *PXo* knockdown conditions. In line with *PXo* knockdown, homozygous *PXo*[PL48] mutant clones were significantly larger and contained more enterocytes than wild-type clones (Extended Data Fig. 2q–u; disruption of *PXo* expression by *PXo*[PL48] mutation confirmed in Extended Data Fig. 2c). Whereas P_i restriction and *PXo* knockdown had synergistic effects in stimulating midgut proliferation (Fig. 1c and Extended Data Fig. 1w), feeding flies with additional P_i could not rescue *PXo* knockdown-induced hyperproliferation (Extended Data Fig. 1w). By contrast, *PXo* overexpression in enterocytes inhibited P_i starvation-induced hyperproliferation (Fig. 1i), despite having no impact on bleomycin-induced hyperproliferation (Extended Data Fig. 1x). Therefore, in response to P_i restriction, suppression of PXo triggers progenitor proliferation and enterocyte production.

To examine endogenous PXo expression, we generated a *PXoGal4* line by CRISPR–Cas9-mediated knock-in, finding stronger expression in enterocytes than in progenitors (Extended Data Fig. 2a,d). In addition, we raised an antibody against the C terminus of PXo (Extended Data Fig. 2e), whose staining appeared as puncta in enterocytes and diminished following *PXo* knockdown (Extended Data Fig. 2f,g). Further, we inserted a hemagglutinin (HA)-based tag at the N terminus of endogenous PXo and observed the same HA staining pattern as with anti-PXo antibody (Extended Data Fig. 2a,h,h'). Although strong endogenous *PXo* expression was also detected in enteroendocrine cells[14] (Extended Data Fig. 2d), *PXo* knockdown in these cells did not induce proliferation (Extended Data Fig. 2v). Moreover, *PXo* knockdown under the control of *DlGal4*[ts], whose expression is restricted to ISCs during homeostasis[15], did not affect proliferation when flies were on normal food (Extended Data Fig. 2w). However, when the midgut was damaged by bleomycin, which is known to accelerate ISC–enteroblast–enterocyte differentiation[10], *DlGal4*[ts]-driven *PXo* knockdown promoted bleomycin-induced proliferation (Extended Data Fig. 2w), suggesting that PXo is required in progenitors when they are actively differentiating. Therefore, PXo is required in enterocytes and differentiating progenitors to suppress midgut proliferation.

In some plants, the epitope-tagged PXo orthologue localizes to the Golgi network and uncharacterized vesicles, whose exocytosis has been proposed as a mechanism of P_i export[16]. Interestingly, both N-terminally tagged GFP–PXo and C-terminally tagged PXo–HA were markers of oval-shaped structures in the fly midgut (Fig. 2a), which were enriched with endogenous PXo (Fig. 2l) and are referred to as PXo bodies. In addition to the midgut, PXo bodies were found in the hindgut (Extended Data Fig. 3a) but were rarely observed in other organs and tissues we examined, including the Malpighian tubules, crop, brain, muscles and germlines (Extended Data Fig. 3b–g). Ultrastructural analysis by electron microscopy (EM) with immunogold labelling in both plastic and frozen midgut sections showed GFP–PXo to be a membrane marker for multilamellar organelles (Fig. 2b–d and Extended Data Fig. 4a). Further, with heat-induced antigen retrieval (HIAR), immunolabelling EM detected the enrichment of endogenous PXo in these multilamellar structures in wild-type midguts (Fig. 2d). Thus, in EM sections of midguts without epitope-tagged PXo expression, PXo bodies could be recognized in both enterocytes and progenitors by their distinct ultrastructural morphology unlike that of canonical organelles[17] (Extended Data Fig. 4b,b'). Characterization of PXo bodies by co-staining
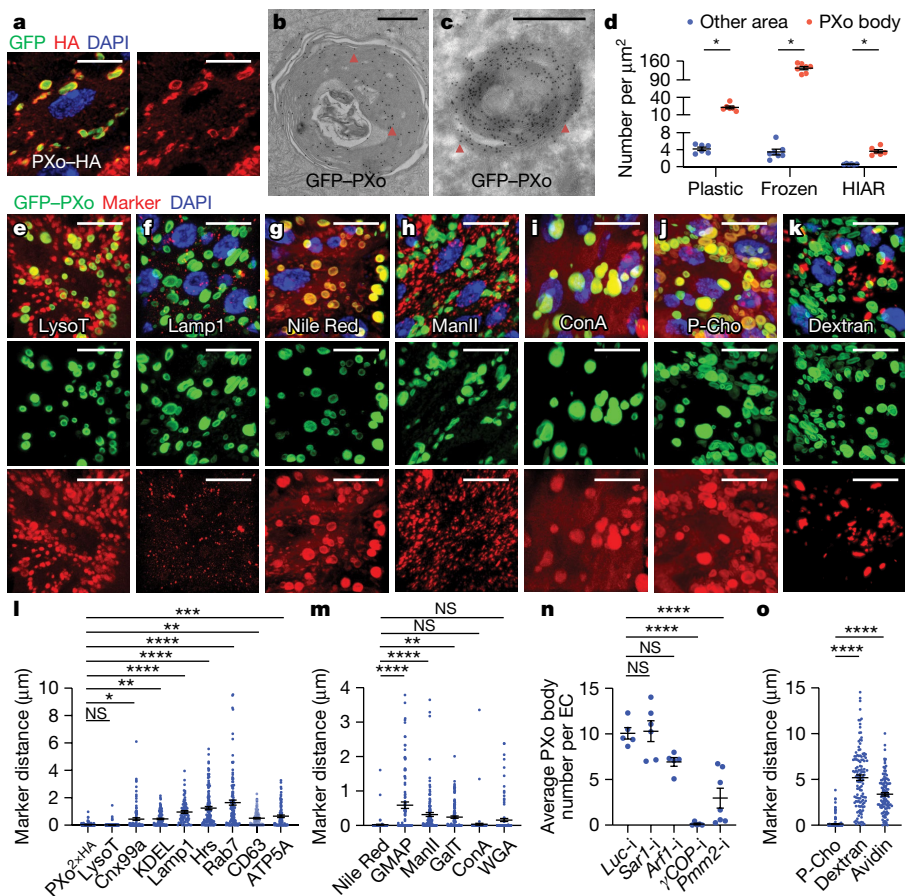
Fig. 2 | PXo localizes to PXo bodies, a type of multilamellar organelle. a, Three-dimensional (3D) view of GFP–PXo and PXo–HA coexpressed in enterocytes. **b,** Midgut EM (plastic section) with immunogold labelling of ubiquitously expressed GFP–PXo. **c,** Midgut EM (frozen section) with immunogold labelling of GFP–PXo expressed in enterocytes. Arrowheads indicate examples of labelled GFP–PXo. **d,** Immunogold labelling density of GFP–PXo or endogenous (with HIAR) PXo. $n = 6$ (plastic; $P = 0.0312$), 7 (frozen; $P = 0.0156$) and 6 (HIAR; $P = 0.0312$) per group. **e–k,** Midguts ubiquitously expressing GFP–PXo were stained for the acidic dye LysoTracker-Red (LysoT) (**e**), the lysosome marker Lamp1 (**f**), the lipid dye Nile Red (**g**), the Golgi marker ManII-TagRFP (**h**), the glycosylation probe ConA (**i**), the phospholipid tracer P-Cho (10 min after injection) (**j**) or the endocytosis marker dextran (**k**). The 3D view is presented at top along with separate views for the green and red channels below.

l,m, Shortest distance between each labelled PXo body and endogenous PXo or other markers. From left to right: $n = 125, 108, 105, 85, 71, 126, 116, 107, 85, 130, 104, 121, 121, 130$ and 121 PXo bodies from 3 analysed midguts; P values are 1.00, 0.0170, 1.68×10^{-3}, 7.00×10^{-9}, $<1 \times 10^{-14}$, $<1 \times 10^{-14}$, 3.94×10^{-3}, 1.17×10^{-4}, $<1 \times 10^{-14}$, 3.28×10^{-5}, 3.59×10^{-3}, 1.00 and 0.178. **n,** Average number of PXo–HA-labelled PXo bodies in enterocytes expressing *Luc* ($n = 5$), *Sar1* ($n = 6$; $P = 1.00$ compared with *Luc*-i), *Arf1* ($n = 5$; $P = 0.109$), *γCOP* ($n = 5$; $P = 5.40 \times 10^{-7}$) or *Pmm2* ($n = 7$; $P = 2.88 \times 10^{-5}$) RNAi reagent for 7 days. **o,** Shortest distance between each labelled PXo body and P-Cho, dextran ($P < 1 \times 10^{-14}$) or avidin ($P < 1 \times 10^{-14}$). $n = 232$ (P-Cho), 127 (dextran) and 113 (avidin) PXo bodies from 4 analysed midguts per group. Data are shown as mean ± s.e.m. P values were calculated by two-tailed Wilcoxon signed-rank test (**d**) or one-way ANOVA with Bonferroni's multiple-comparison test (**l–o**). Scale bars, 10 μm (**a**,**e–k**) and 1 μm (**b**,**c**).

showed that they were acidic (Fig. 2e,l) but did not colocalize with markers for the endoplasmic reticulum (ER) (Fig. 2l and Extended Data Fig. 3h,i; often in proximity and occasionally in direct contact), lysosome (Fig. 2f,l), endosome (Fig. 2l and Extended Data Fig. 3j,k), exosome (Fig. 2l) or mitochondria (Fig. 2l and Extended Data Fig. 3l). Whereas PXo bodies are one type of subcellular structure that was positive for staining with the lipid dye Nile Red (Fig. 2g,m), their ultrastructural morphology differed from that of lipid droplets[17] (Extended Data Fig. 4c). Interestingly, PXo bodies were found in proximity to, but did not colocalize with, *cis*-, medial- and *trans*-cisternae markers (GMAP, ManII and GalT, respectively) for the Golgi body (Fig. 2h,m and Extended Data Fig. 3m,n,s). Moreover, co-staining of GFP–PXo with the lectins concanavalin A (ConA) and wheat germ agglutinin (WGA) demonstrate PXo body glycosylation (Fig. 2i,m and Extended Data Fig. 3o), which is probably mediated by the Golgi apparatus.

To further investigate PXo body biogenesis, we examined whether disruption of canonical organelles could affect PXo bodies. Knockdown of *Sar1* or *Arf1*, the canonical GTPases that mediate anterograde or retrograde ER–Golgi vesicle trafficking, respectively[18], and that maintain the normal morphology of the ER, Golgi body[19] and lipid droplets[20], had no

significant impact on the morphology and density of PXo–HA-labelled PXo bodies in enterocytes (Fig. 2n and Extended Data Fig. 4f–h). By contrast, knockdown of *γCOP*[21], which is essential for protein transport from the Golgi body, or knockdown of *Pmm2* (ref. 22), which encodes a critical enzyme for *N*-glycosylation, markedly diminished the number of PXo bodies (Fig. 2n and Extended Data Fig. 4i,j). In line with immunostaining, EM images of midguts with *γCOP* knockdown showed fragmented and depleted PXo bodies (Extended Data Fig. 4d,e). Moreover, *Lamp1* knockdown, which inhibits lysosomal maturation[23], resulted in a modest increase in average PXo body size (Extended Data Fig. 4k,n,q), whereas no apparent impact on PXo bodies was observed following the expression of validated RNAi reagents to knock down components required for mitochondrial fission and fusion (*Pink1* and *Parkin*)[24], endosome formation (*Rab7*)[25], endosome recycling or exosome secretion (*Rab11*)[26] (Extended Data Fig. 4k–m,q–v). To further explore the origin of PXo bodies, we traced two main sources of the endomembrane system, that is, membrane synthesis and endocytosis. Following injection of a choline analogue, propargylcholine (P-Cho), we could visualize phospholipids newly synthesized from the ER, which strongly
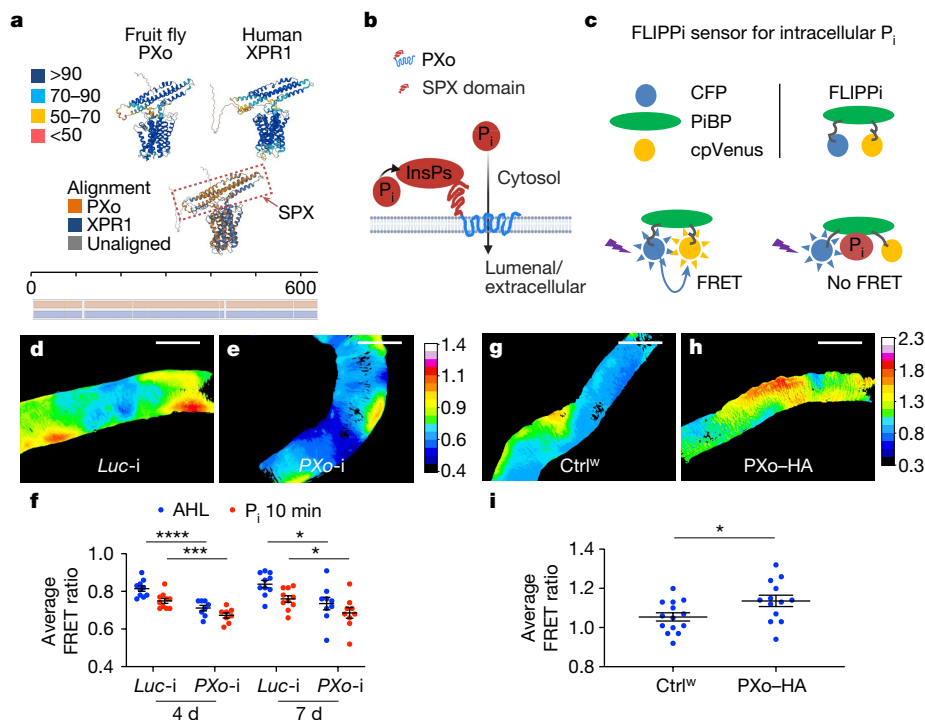
Fig. 3 | PXo regulates cytosolic P$_i$ levels. a, AlphaFold structure prediction of fly PXo and its human orthologue XPR1, with colour-scaled visualization of the prediction confidence score (0–100). A pairwise structure alignment is shown below, with aligned regions superposed on one another and highlighted in colour. A summary of the amino acid sequence alignment is shown at the bottom, with aligned regions highlighted in colour. The P$_i$-sensing SPX domain is highlighted by the dashed box. **b**, Model of the mechanism of action of PXo in P$_i$ transport. The diagram was created using BioRender.com. **c**, Binding of P$_i$ to the P$_i$-binding protein (PiBP) domain causes conformational changes in the chimeric FLIPPi reporter, increasing the distance between the donor and acceptor fluorescent proteins and hence reducing FRET ratios. **d**,**e**, Colour-scaled FRET ratio visualization of enterocytes expressing FLIPPi together with *Luc* (**d**) or *PXo* (**e**) RNAi reagent for 4 days. **f**, FRET ratio quantification for midguts expressing FLIPPi together with *Luc* or *PXo* RNAi reagent in enterocytes for 4 or 7 days, with or without P$_i$ addition to the imaging buffer. AHL, adult haemolymph-like buffer. $n = 10$ (*Luc*-i 4 d, *Luc*-i 7 d), 8 (*PXo*-i 4 d) and 9 (*PXo*-i 7 d) midguts analysed per group. P values from left to right: 4.57×10^{-5}, 4.34×10^{-4}, 0.0121 and 0.0405. **g**–**i**, FRET ratio visualization (**g**,**h**) and quantification (**i**) for enterocytes expressing FLIPPi alone ($n = 14$) or FLIPPi together with PXo–HA ($n = 13$) for 7 days. $P = 0.0278$. Data are shown as mean ± s.e.m. P values obtained by two-tailed Mann–Whitney U test (**f**,**i**). Scale bars, 200 μm (**d**,**e**,**g**,**h**).

co-stained with GFP–PXo at 10 min or 2 h after injection (Fig. 2j,o and Extended Data Fig. 3p,q,t). By contrast, endocytosis vesicles visualized by Texas Red-labelled dextran or avidin did not colocalize with GFP–PXo (Fig. 2k,o and Extended Data Fig. 3r,t). Therefore, the PXo body is an active deposit of newly synthesized phospholipids and a distinct compartment of the endomembrane system that depends on Golgi protein transport and glycosylation for its biogenesis.

PXo is highly conserved, with orthologues across species from yeast to humans. On the basis of AlphaFold structure prediction[27] and previous literature[12] (Fig. 3a), PXo contains eight-pass transmembrane α-helical barrels (EXS domain) that probably form the pore for P$_i$ trafficking and an N-terminal SPX domain that faces the cytosol and confers a gating mechanism on intracellular P$_i$ levels by undergoing conformational change following binding to P$_i$-derived InsPs. The PXo structure is remarkably similar to the AlphaFold-predicted structures for the human orthologue XPR1 (Fig. 3a) and the rice orthologue PHO1-2 (Extended Data Fig. 5a), both previously demonstrated to mediate P$_i$ efflux away from the cytosol in radiolabelled P$_i$ tracing[28] or patch clamp[29] experiments. Inferred from the activity of these orthologues, PXo is expected to mediate P$_i$ transport from the cytosol into PXo bodies (Fig. 3b), given its predominant localization to the membranes of PXo bodies (Fig. 2b,c). To confirm the physiological relevance of PXo in P$_i$ regulation, we examined cytosolic P$_i$ levels with a Förster resonance energy transfer (FRET)-based P$_i$ sensor, cpFLIPPi-6.4 (referred to as FLIPPi)[2]. FLIPPi was expressed in the cytosol and was not present within PXo bodies (Extended Data Fig. 5b,c). The FRET ratio of FLIPPi is taken as the fluorescence ratio of cpVenus versus cyan fluorescent protein

(CFP), which inversely correlates with cytosolic P$_i$ levels (Fig. 3c). We dissected midguts expressing FLIPPi and measured the FRET ratios in live tissues. As a proof of principle, addition of 30 mM P$_i$ to the imaging buffer decreased FRET ratios in the whole midgut, in progenitor cells and in enterocytes (Extended Data Fig. 5d–h and Supplementary Video 1; different Gal4 lines were used to drive FLIPPi expression), whereas PFA feeding increased FRET ratios (Extended Data Fig. 5h). Moreover, *MFS10* knockdown increased FRET ratios in enterocytes (Extended Data Fig. 5i–k), which is expected because MFS10 mediates P$_i$ uptake[8]. Notably, *PXo* knockdown decreased FRET ratios in enterocytes (Fig. 3d–f and Extended Data Fig. 5l–n; two different RNAi lines examined), whereas both enterocytes and progenitors with PXo overexpression exhibited increased FRET ratios (Fig. 3g–i and Extended Data Fig. 5o–q). *PXo* knockdown in progenitors did not affect FRET ratios (Extended Data Fig. 5q), which might be due to the relatively low abundance of PXo (Extended Data Fig. 2d) and PXo bodies (Extended Data Fig. 4b) in progenitors. In conclusion, PXo transports cytosolic P$_i$ into PXo bodies, which is critical to restrict cytosolic P$_i$ levels in enterocytes.

To explore how PXo bodies are affected by P$_i$ availability and *PXo* expression, we examined their morphology and abundance in response to P$_i$ starvation or other challenges. Notably, whereas unlabelled PXo bodies were mostly 0.15–3 μm in diameter in the EM sections of a healthy midgut, they were significantly smaller following PFA-induced or *MFS10* knockdown-induced P$_i$ starvation (Fig. 4a,b,d and Extended Data Fig. 6a–f) and larger when flies were fed additional P$_i$ (Fig. 4d). Moreover, PXo bodies were smaller and often engulfed by lysosomes in midguts with *PXo* knockdown (Fig. 4c,d and Extended Data Fig. 6g–i; two
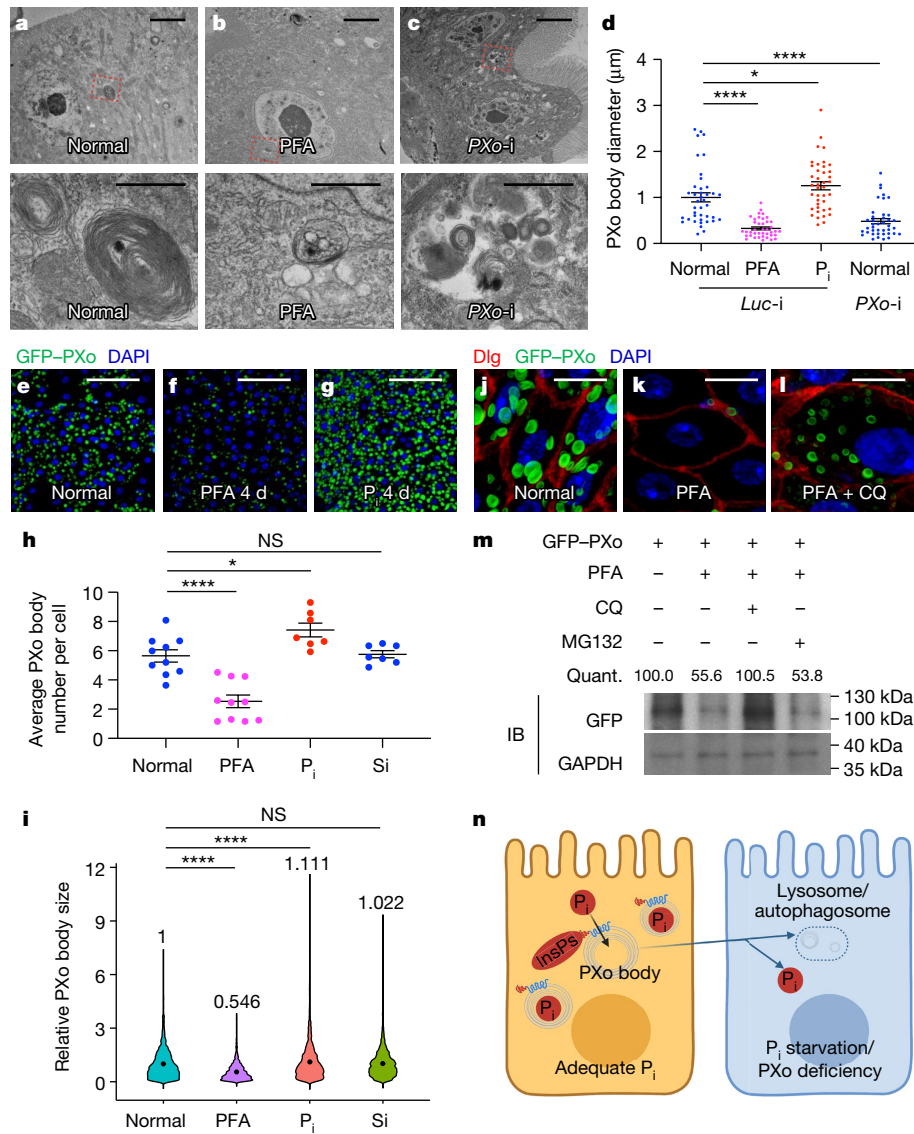
Fig. 4 | PXo bodies are sensitive to P_i availability. a–c, EM images of midguts ubiquitously expressing *Luc* or *PXo* RNAi reagent for 5 days, with or without PFA for the last 4 days. Bottom, magnified views of the highlighted regions. **d**, PXo body diameter in EM sections of midguts ubiquitously expressing *Luc* (with normal food, 4 days of PFA or 4 days of P_i) or *PXo* RNAi reagent for 5 days. $n = 40$ per group. *P* values from bottom to top: 3.00×10^{-9}, 0.0465, 4.34×10^{-6}. **e–g**, Midguts with ubiquitous GFP–PXo expression for 7 days, on normal food (**e**), 4 days of PFA (**f**) or 4 days of P_i (**g**). **h**, Quantification of average PXo body number per cell. **i**, Relative PXo size presented as violin plots with mean values. A sodium sulfate (Si) group was added to control for anion concentrations in P_i food. $n = 10$ (normal), 10 (PFA), 7 (P_i) and 7 (Si) midguts analysed. *P* values from bottom to top in **h**: 9.88×10^{-6}, 0.0183, 1.00. $n = 2{,}289$ (normal), 1,113 (PFA), 2,082 (P_i) and 1,975 (Si) PXo bodies analysed. *P* values from bottom to top in **i**: $<1 \times 10^{-14}$, 3.88×10^{-5}, 1.00. **j–l**, Midguts from flies with ubiquitous GFP–PXo expression fed normal food (**j**), 2 days of PFA (**k**) or 2 days of PFA + CQ (**l**). **m**, Immunoblot (IB) analysis of lysates from the midguts of flies expressing GFP–PXo fed normal food, 2 days of PFA, 2 days of PFA + CQ or 2 days of PFA + MG132. GAPDH was the loading control. Relative normalized anti-GFP immunoblot intensity is quantified. Gel source data are provided in Supplementary Fig. 1a. Quant., quantification. **n**, How PXo bodies transport P_i and respond to P_i starvation or *PXo* knockdown. The diagram was created using BioRender.com. Quantitative data (except in violin plots and western blots) are shown as mean ± s.e.m. *P* values were obtained by one-way ANOVA with Bonferroni's multiple-comparisons test (**d,h,i**). Scale bars, 4 μm (**a–c**, top images); 1 μm (**a–c**, bottom images); 50 μm (**e–g**); 10 μm (**j–l**).

different RNAi lines examined). In line with EM observations, GFP–PXo-labelled PXo bodies increased in number and size when flies were fed excessive P_i but were diminished when flies were fed PFA (Fig. 4e–i and Extended Data Fig. 7a–c). In addition, by feeding flies CDF, we confirmed that PXo bodies were progressively diminished as we lowered the dietary P_i concentration to 20% and 10% of the standard level (Extended Data Fig. 7d–f). Following P_i starvation, endogenous *PXo* mRNA levels and protein staining were lower (Fig. 1d and Extended Data Fig. 7g–j), while the residual endogenous PXo puncta were often engulfed by enlarged lysosomes and induced autophagosomes (Extended Data Fig. 7i,j). Further, PFA-induced degradation of GFP–PXo and PXo bodies could be rescued by treatment with the lysosome/autophagosome inhibitors bafilomycin A1 (BafA1) and chloroquine (CQ) but not the proteasome inhibitor MG132, as demonstrated in S2R+ cells in vitro (Extended Data Fig. 7k–n) or in the midgut in vivo (Fig. 4j–m). Because the SPX domain can adopt different conformations depending on cytosolic P_i levels[12], we asked whether it confers the P_i sensitivity of PXo expression. Interestingly, the expression and staining pattern of an SPX-truncated version of PXo in the midgut, despite being more diffuse than that for full-length PXo, was not affected by PFA (Extended Data
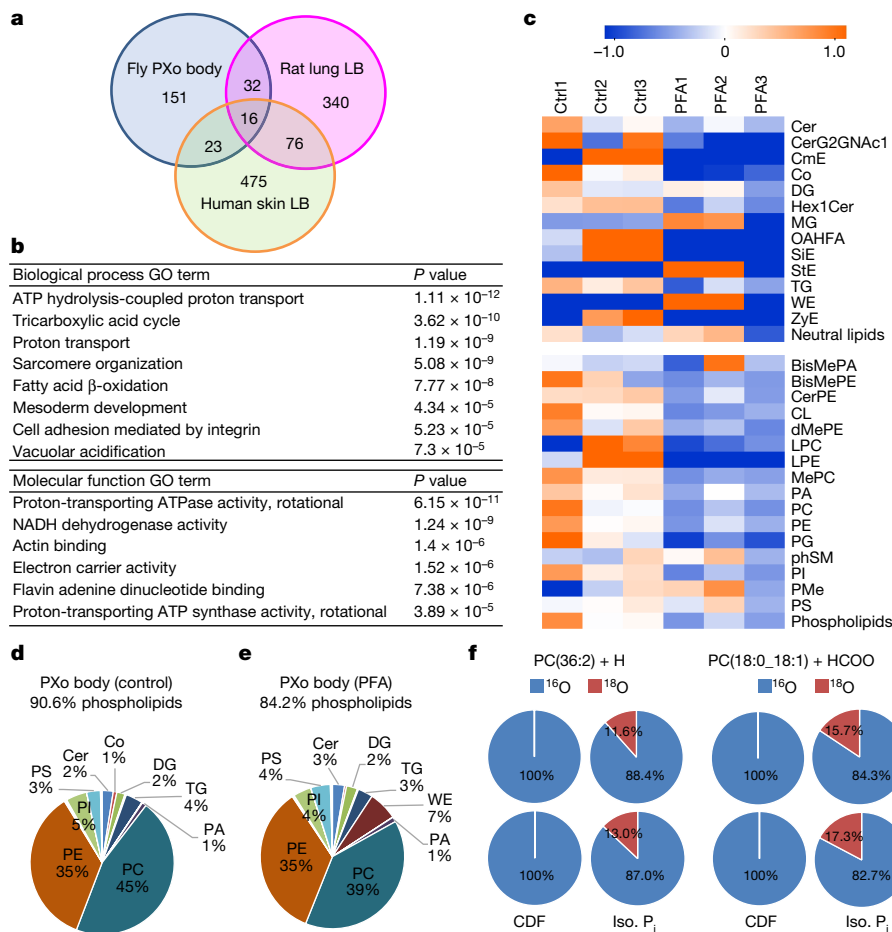
Fig. 5 | Proteomic and lipidomic characterization of PXo bodies. a, Venn diagram illustrating the difference and commonality between the proteomes of PXo bodies and mammalian lamellar bodies (LBs). In total, 248 identified PXo body proteins mapped to 222 unique mammalian orthologues (9 without predicted orthologues), of which 151 have not been found in mammalian lamellar bodies in previous studies. **b**, Top enriched biological process and molecular function GO terms for the PXo body proteome listed by the rank of *P* values based on DAVID GO analysis. **c**, Heatmap of the total ion intensity (indicative of molar quantity) of major lipid classes identified in PXo bodies from flies fed normal food or PFA for 2 days, with three biological replicates per condition. The scaled colours are presented as the $\log_2$(fold change) relative to the average for each row. Neutral lipids and phospholipids are highlighted by the upper and lower brackets, respectively, with their sum listed below each bracket. The full name and content of each lipid class can be found in Supplementary Table 2. **d,e**, Average values of three biological replicates were used to calculate the representation of different lipid categories in PXo bodies from flies fed with normal food (**d**) or PFA for 2 days (**e**). Lipid categories that make up 1% or more of the total molar quantity are labelled in the pie charts. Lipid classification here is more general than in **c** for convenient comparison with previously published lipidomic analyses (see Supplementary Table 2 for details). **f**, Percentage of ^{16}O-only or ^{18}O-labelled PC lipids detected in midgut PXo bodies from control or isotopic P_i-traced flies (two biological replicates per condition; see 'Peak area' in Supplementary Table 2c for details). Iso., isotope.

Fig. 7o–q). Therefore, PXo bodies depend on P_i and PXo expression for biogenesis and maintenance and undergo SPX-dependent lysosomal/autophagosomal degradation following P_i starvation (Fig. 4n).

Morphologically similar multilamellar organelles have been reported as lamellar bodies in various mammalian cell types, including lung alveolar type II cells[30] and keratinocytes[31]. Lamellar bodies are secretory lysosomes that require the Golgi apparatus for biogenesis[32,33] and contribute to the lipid-rich protective barriers covering the alveolar/gastric lining or the skin surface[33,34]. In the mammalian lung, the lysosome-associated membrane protein LAMP3 (ref. 35) and the lipid transporter ATP-binding cassette transporter A3 (ABCA3)[36] are essential for lamellar body biogenesis. However, on the basis of the 'Smurf' assay, intestinal barrier integrity appears normal in flies with prolonged ubiquitous expression of *PXo* RNAi reagent (Extended Data Fig. 8a,b), whereas expression of validated RNAi reagents for *Drosophila Lamp1* (a LAMP3 orthologue) or *Abca3* did not impair PXo body morphology (Extended Data Fig. 4n–q). Therefore, the PXo body appears to differ from previously characterized lamellar bodies in its biogenesis and function.

For systematic profiling of the molecular and biochemical properties of PXo bodies, we developed a protocol to extract them from fly guts. After ultracentrifugation of midgut homogenates with an OptiPrep floating gradient, GFP–PXo-labelled PXo bodies were enriched in fractions with a density of ~1.11–1.14 g ml^{-1} (Extended Data Fig. 9a–f), heavier than the previously reported density of ~1.059–1.070 g ml^{-1} of mammalian lamellar bodies[37]. Although the dissociated PXo bodies appeared intact on the basis of ultrastructural analysis, they could not be separated by gradient fractionation from mitochondria and other organelles in the endomembrane system owing to their similar density (Extended Data Fig. 9g,h). Thus, we adapted an immunoprecipitation protocol to specifically pull down GFP–PXo-labelled PXo bodies using Chromotek-GFP-Trap agarose beads (Extended Data Fig. 9i–n). Proteomic analysis of purified PXo bodies with high-resolution liquid chromatography followed by tandem mass spectrometry (LC–MS/MS) uncovered 248 unique proteins, whose 222 mammalian orthologues overlapped very little with proteins previously identified in lamellar bodies from the rat lung[38,39] or human epidermis[40] (Fig. 5a). Neither lung nor epidermal lamellar bodies contained the mammalian orthologue

of PXo. Conversely, the *Drosophila* midgut PXo body proteome did not include the orthologues for general lamellar body markers (CAV1, FLOT1, FLOT2 or LAMP proteins)[35,40,41], the lung lamellar body marker (ABCA3)[38] or the epidermal lamellar body marker (DMKN)[40] (Supplementary Table 1). Assuming that GFP–PXo labelling does not affect the basic composition of PXo bodies, our data suggest that the PXo body proteome is different from those of previously reported lamellar bodies. By co-immunostaining, we confirmed the localization of many identified candidates to PXo bodies as well as other subcellular compartments with which they were previously known to be associated (Extended Data Fig. 10a–f,i). In addition, we confirmed the localization of several metabolic enzymes to PXo bodies (Treh, Ance and Mipp1; Extended Data Fig. 10g,h,j). Gene ontology (GO) analysis of the PXo body proteome identified distinct features with three major enriched categories (Fig. 5b): (1) proton pump/vacuolar acidification (multiple V-type ATPases), which explains the acidity of PXo bodies; (2) cytoskeleton-binding and actin motor proteins, which might regulate the shape and distribution of PXo bodies; and (3) citric acid and fatty acid metabolism, which might provide the metabolic intermediates and energy for PXo body biogenesis.

To better understand the biochemical properties of PXo bodies, the lipidome of purified PXo bodies was analysed using semi-quantitative label-free high-resolution LC–MS/MS. In total, 576 lipid species were detected in PXo bodies representing 29 classes (Fig. 5c and Supplementary Table 2). The molar ratio of phospholipids to total lipids was 90.6% in PXo bodies (Fig. 5d), much greater than the reported measurements for the whole midgut or fly body[42,43] (Extended Data Fig. 8c,d). The most enriched class of lipids in PXo bodies was phosphatidylcholine (PC) (Fig. 5d). By contrast, phosphatidylethanolamine (PE) was the most prominent phospholipid in *Drosophila* membranes in general[43], whereas the most abundant lipids in mammalian lung and epidermal lamellar bodies were dipalmitoyl PC (DPPC)[34] and free sterols[44], respectively. Interestingly, flies fed excessive PC had larger and a greater number of PXo bodies (Extended Data Fig. 8e–h), suggesting that PXo bodies might be a major intracellular deposit for phospholipids, especially PC. Notably, following short-term P_i starvation and before apparent PXo body degradation (Extended Data Fig. 9o,p), the PXo body lipidome changed markedly, with a decrease in total phospholipids but not neutral lipids (Fig. 5c). Notably, PC representation in the PXo body lipidome dropped from 45% to 39% after PFA feeding for 2 days (Fig. 5d,e). Moreover, when we fed flies CDF containing ^{18}O isotope-labelled P_i, ^{18}O incorporation into PC lipids was detected by stable isotopic tracing high-resolution LC–MS/MS analysis of purified PXo bodies (Fig. 5f). Therefore, P_i consumed by the PXo body can be converted and stored in the form of phospholipids, with the prominent phospholipid composition of PXo bodies undergoing remodelling following P_i starvation.

To unravel the signalling mechanism of P_i starvation and *PXo* knockdown, we performed affinity purification and LC–MS/MS analysis of PXo-interacting proteins. In line with our immunostaining and proteomic profiling of PXo bodies, the top candidates interacting with GFP–PXo (Fig. 6a and Supplementary Table 3) were proteins related to the Golgi apparatus (for example, γCOP, εCOP and βCOP), vacuolar acidification (for example, Vha68-2, Vha55 and Vha26) and phospholipid metabolism (for example, Ost48, Vap33 and Inos). In addition, our candidate PXo-interacting proteins (Fig. 6a) included multiple components of the Striatin-interacting phosphatase and kinase (STRIPAK) complex, such as Cka, microtubule star (mts) and protein phosphatase 2A at 29B (Pp2A-29B). Interestingly, two *Drosophila* STRIPAK core components, Cka and MOB kinase activator 4 (Mob4), scored as top PXo interactors in a previous high-throughput yeast two-hybrid study[45].

STRIPAK is an evolutionarily conserved protein complex that regulates vesicular transport, endomembrane organization and a variety of signalling pathways[3]. In *Drosophila*, core components of STRIPAK include Cka (a scaffold protein and the only Striatin in *Drosophila*), mts, Pp2A-29B,
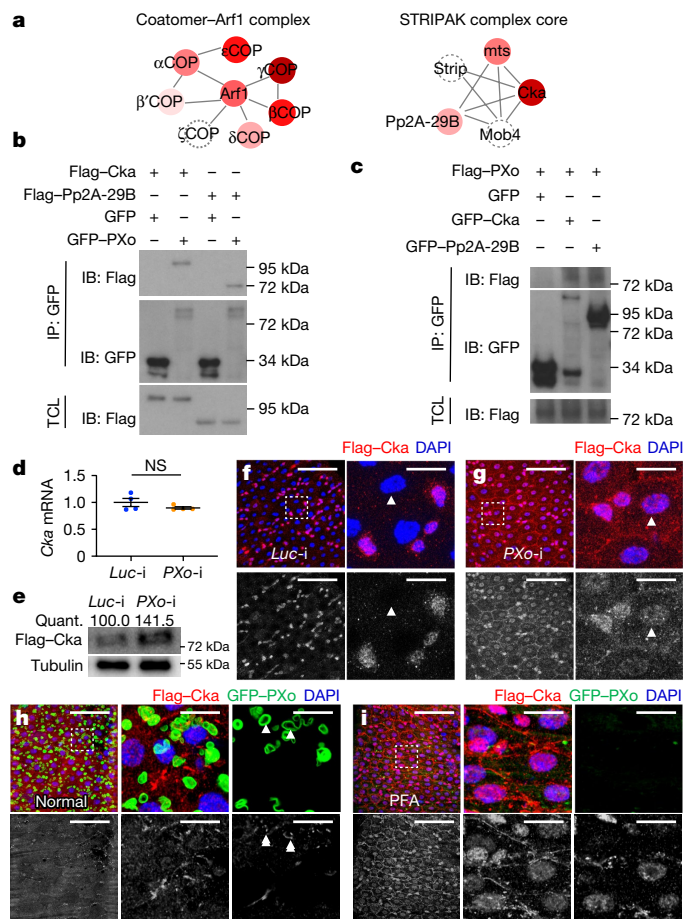

Fig. 6 | PXo interacts with STRIPAK core components and suppresses Cka in enterocytes. a, Top complexes enriched for PXo-interacting proteins identified by affinity purification and LC–MS/MS. Edges represent interactions among complex members. Node colours reflect the ratios of identified peptide number (PN) between the experimental (GFP–PXo) and control (GFP) groups, with the darkness of red indicating (PN(GFP–PXo) + 1)/(PN(GFP) + 1). Grey circled nodes represent proteins not captured by LC–MS/MS. **b,c**, Extracts from S2R⁺ cells expressing GFP or GFP-tagged PXo, Cka or Pp2A-29B were subjected to immunoprecipitation (IP) with GFP-Trap beads. TCL, total cell lysate. Gel source data are provided in Supplementary Fig. 1b,c. **d**, RT–qPCR measurement of *Cka* mRNA in midguts with ubiquitous expression of *Luc* or *PXo* RNAi reagent for 5 days. *n* = 4 biological replicates per group. Data are shown as mean ± s.e.m. The *P* value (0.276) is from a two-tailed Welch's *t*-test. **e**, Immunoblot analysis of midguts with ubiquitous expression of Flag–Cka along with *Luc* or *PXo* RNAi reagent for 5 days. Samples of the same volume in parallel wells of the same gel were blotted for tubulin as a control. Relative normalized anti-Flag immunoblot intensity is quantified. Gel source data are provided in Supplementary Fig. 1d. **f,g**, Flag–Cka staining of midguts expressing *Luc* (**f**) or *PXo* (**g**) RNAi reagent in enterocytes for 4 days. Right, magnified views of the boxed regions; example enterocytes are highlighted by arrowheads. **h,i**, Flag–Cka and GFP–PXo co-staining of midguts from flies fed normal (**h**) or PFA (**i**) food for 7 days. Right two columns, magnified views of highlighted regions, with a single *z* stack of separate channels shown on the right and arrowheads indicating colocalization. The red channel corresponding to anti-Flag staining is shown in greyscale below the merged images in **f**–**i**. Scale bars, 50 μm (**f**–**i**) and 10 μm (**f**–**i**, magnified views).

Mob4 and Striatin-interacting protein (Strip). We first validated direct PXo–Cka and PXo–Pp2A-29B interactions by co-immunoprecipitation (Fig. 6b,c). Notably, whereas *PXo* knockdown in enterocytes did not affect *Cka* expression at the mRNA level (Fig. 6d), it increased the protein abundance of Flag-tagged Cka expressed under the control of a ubiquitous promoter (*tub*-Flag–Cka), as measured by western blot analysis
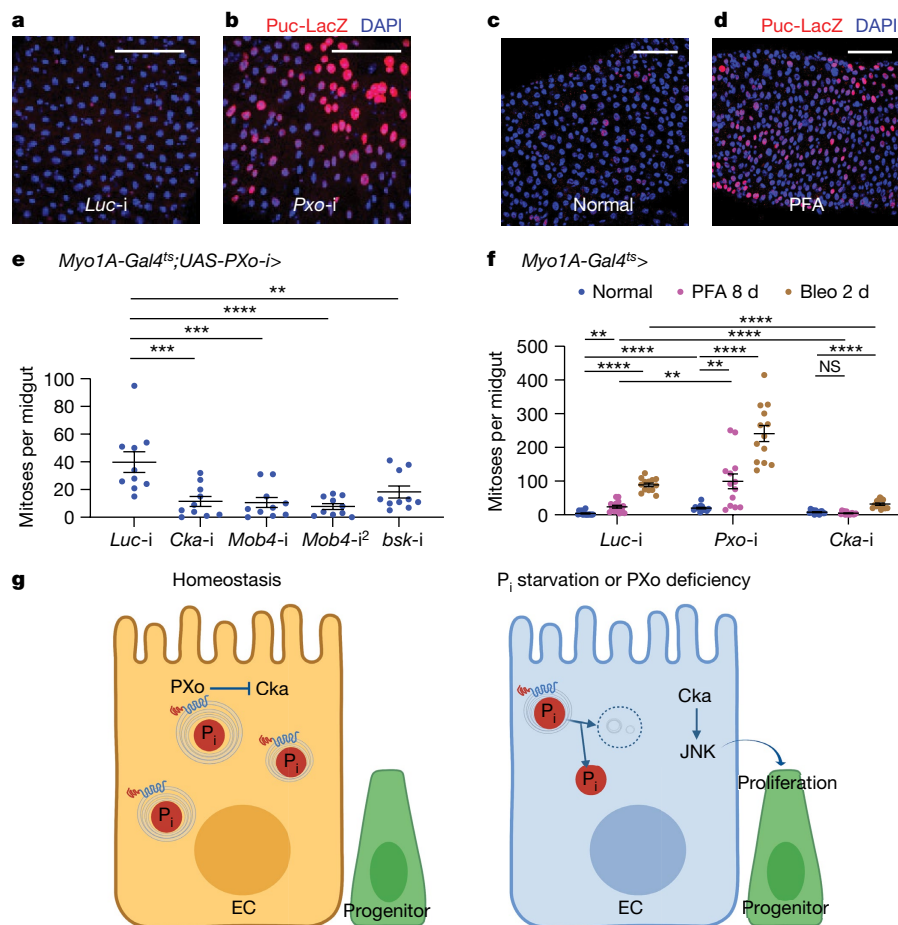
Fig. 7 | STRIPAK/Cka–JNK signalling mediates the hyperproliferation induced by P_i starvation or *PXo* knockdown. a,b, Puc-LacZ staining of midguts expressing *Luc* (**a**) or *PXo* (**b**) RNAi reagent in enterocytes for 7 days. Enterocytes have large nuclei identified by DAPI staining. **c,d**, Puc-LacZ staining of midguts from flies fed normal (**c**) or PFA (**d**) food for 7 days. **e**, Mitosis quantification in midguts expressing *PXo* RNAi reagent together with *Luc*, *Cka*, *Mob4* (two different lines) or *bsk* RNAi reagent in enterocytes for 8 days. $n = 10$ midguts per group. P values from bottom to top: 3.12×10^{-4}, 2.10×10^{-4}, 4.87×10^{-5} and 7.53×10^{-3}. **f**, Mitosis quantification in midguts of flies expressing *Luc*, *PXo* or *Cka* RNAi reagent in enterocytes for 8 days and fed normal food ($n = 14, 13, 13$), PFA ($n = 15, 13, 14$) or bleomycin for the last 2 days ($n = 13, 13, 13$). P values from

left to right: 1.70×10^{-3}, $<1 \times 10^{-14}$, 1.70×10^{-5}, 2.10×10^{-3}, 9.83×10^{-3}, 1.18×10^{-9}, 3.83×10^{-5}, 1.92×10^{-7}, 0.101 and 2.87×10^{-8}. **g**, A schematic summary of the connections between P_i storage, PXo and P_i signalling. PXo transports P_i into PXo bodies and antagonizes Cka–JNK signalling. The coupling of both roles in PXo, whose conformation and activity are sensitive to cytosolic P_i levels, activates mitogenic JNK signalling under pathological conditions of P_i starvation or *PXo* deficiency. The diagram was created using BioRender.com. Data are shown as mean ± s.e.m. P values are from one-way ANOVA with Bonferroni's multiple-comparisons test in **e** and within the same genotype in **f** or from a two-tailed Mann–Whitney U test between different genotypes in **f**. Scale bars, 50 μm (**a–d**).

(Fig. 6e). As shown by immunostaining, whereas Flag–Cka is normally expressed at very low levels in enterocytes (Fig. 6f and Extended Data Fig. 11a,a'; note that enterocytes are polyploid and have large nuclei), it exhibited increased expression and nuclear accumulation in enterocytes (Fig. 6f,g) and in progenitors that were differentiating towards enterocytes (Extended Data Fig. 11a,b,a',b') following *PXo* knockdown. In line with our results using *tub*-Flag–Cka, enterocyte-specific expression of blue fluorescent protein (BFP)-tagged Cka (BFP–Cka) was barely detectable unless *PXo* was downregulated by RNAi (Extended Data Fig. 11c–f), whereas progenitor-specific BFP–Cka could accumulate and localize to the nucleus (Extended Data Fig. 11g,h). Moreover, Flag–Cka often colocalized with GFP–PXo and was even encased by PXo bodies in enterocytes (Fig. 6h). As after *PXo* knockdown, Flag–Cka staining markedly increased and accumulated in the nucleus when PXo bodies degenerated following P_i starvation (Fig. 6i). Altogether, our results suggest that PXo interacts with Cka and antagonizes Cka expression through post-translational sequestration in enterocytes.

Cka can recruit JNK pathway components to facilitate the activation of JNK[3], which is a stress-related mitogen-activated protein kinase (MAPK) known to act non-autonomously in enterocytes to induce progenitor

proliferation[46]. Using the JNK reporter Puc-LacZ[47], we observed strong JNK induction in enterocytes and progenitors that were proliferating and differentiating towards enterocytes following *PXo* knockdown (Fig. 7a,b and Extended Data Fig. 12a,b) or P_i starvation (Fig. 7c,d). By contrast, p38, another stress-related MAPK in the midgut[48], was not induced by *PXo* knockdown (Extended Data Fig. 12c–e). Furthermore, RNAi lines targeting *Cka*, the JNK pathway kinase *bsk* and several other core STRIPAK genes (*Mob4*, *Strip* and *mts*) all rescued the hyperproliferation induced by *PXo* knockdown in enterocytes (Fig. 7e and Extended Data Fig. 12f,g) and progenitors (Extended Data Fig. 12h–j). By contrast, *Pp2A-29B* knockdown in enterocytes enhanced *PXo* knockdown-induced hyperproliferation (Extended Data Fig. 12g), which could be due to promiscuous Pp2A functions such as a role in JNK inhibition[49]. Finally, midguts with *Cka* knockdown in enterocytes did not undergo hyperproliferation following P_i starvation, despite maintaining a dampened proliferative response to tissue damage (Fig. 7f). Altogether, our data suggest that P_i starvation or *PXo* knockdown triggers downstream Cka–JNK signalling to induce midgut hyperproliferation.

In summary, our study identifies the PXo body as pivotal for maintaining cytosolic P_i levels and connecting P_i regulation to tissue homeostasis

(Fig. 7g). With adequate P$_i$ uptake, cytosolic P$_i$ is transported by PXo into PXo bodies and probably consumed for phospholipid synthesis. Conversely, with P$_i$ starvation, PXo expression is downregulated at both the mRNA and protein level and PXo bodies disassemble and decrease in phospholipid content, releasing P$_i$ back into the cytosol. In addition to its function as a P$_i$ transporter, PXo antagonizes the STRIPAK complex protein Cka. Thus, when P$_i$ starvation causes degradation of PXo bodies, Cka–JNK signalling is activated to induce regenerative activities (Fig. 7g).

In unicellular organisms, P$_i$ is indicative of environmental nutrient abundance and generally supports cell growth and division[1]. In metazoans, however, P$_i$ availability is affected by nutrient uptake, systemic metabolism and local P$_i$ usage, thus implicating more complex P$_i$ signalling[50]. In this study, we demonstrated that P$_i$ starvation or *PXo* deficiency induces hyperproliferation and enterocyte differentiation in the epithelium of the *Drosophila* midgut, which might be a compensatory mechanism to produce more enterocytes capable of P$_i$ absorption. Given the scarcity of knowledge about cytosolic P$_i$ regulation in animal cells, our findings might have broad implications and open new avenues for studying P$_i$ metabolism and signalling.

Online content

1. Qi, W., Baldwin, S. A., Muench, S. P. & Baker, A. Pi sensing and signalling: from prokaryotic to eukaryotic cells. *Biochem. Soc. Trans.* **44**, 766–773 (2016).
2. Banerjee, S., Versaw, W. K. & Garcia, L. R. Imaging cellular inorganic phosphate in Caenorhabditis elegans using a genetically encoded FRET-based biosensor. *PLoS ONE* **10**, e0141128 (2015).
3. Hwang, J. & Pallas, D. C. STRIPAK complexes: structure, biological function, and involvement in human diseases. *Int. J. Biochem. Cell Biol.* **47**, 118–148 (2014).
4. Brown, M. R. & Kornberg, A. Inorganic polyphosphate in the origin and survival of species. *Proc. Natl Acad. Sci. USA* **101**, 16085–16087 (2004).
5. Liu, T. Y. et al. Identification of plant vacuolar transporters mediating phosphate storage. *Nat. Commun.* **7**, 11095 (2016).
6. Rao, N. N., Gomez-Garcia, M. R. & Kornberg, A. Inorganic polyphosphate: essential for growth and survival. *Annu. Rev. Biochem.* **78**, 605–647 (2009).
7. Tjellstrom, H., Andersson, M. X., Larsson, K. E. & Sandelius, A. S. Membrane phospholipids as a phosphate reserve: the dynamic nature of phospholipid-to-digalactosyl diacylglycerol exchange in higher plants. *Plant Cell Environ.* **31**, 1388–1398 (2008).
8. Bergwitz, C. et al. Roles of major facilitator superfamily transporters in phosphate response in Drosophila. *PLoS ONE* **7**, e31730 (2012).
9. Micchelli, C. A. & Perrimon, N. Evidence that stem cells reside in the adult Drosophila midgut epithelium. *Nature* **439**, 475–479 (2006).
10. Amcheslavsky, A., Jiang, J. & Ip, Y. T. Tissue damage-induced intestinal stem cell division in Drosophila. *Cell Stem Cell* **4**, 49–61 (2009).
11. Xu, C. et al. An in vivo RNAi screen uncovers the role of AdoR signaling and adenosine deaminase in controlling intestinal stem cell activity. *Proc. Natl Acad. Sci. USA* **117**, 464–471 (2020).
12. Wild, R. et al. Control of eukaryotic phosphate homeostasis by inositol polyphosphate sensor domains. *Science* **352**, 986–990 (2016).
13. Wege, S. et al. The EXS domain of PHO1 participates in the response of shoots to phosphate deficiency via a root-to-shoot signal. *Plant Physiol.* **170**, 385–400 (2016).
14. Hung, R. J. et al. A cell atlas of the adult Drosophila midgut. *Proc. Natl Acad. Sci. USA* **117**, 1514–1523 (2020).
15. Zeng, X., Chauhan, C. & Hou, S. X. Characterization of midgut stem cell- and enteroblast-specific Gal4 lines in drosophila. *Genesis* **48**, 607–611 (2010).
16. Arpat, A. B. et al. Functional expression of PHO1 to the Golgi and trans-Golgi network and its role in export of inorganic phosphate. *Plant J.* **71**, 479–491 (2012).
17. Xu, C., Ericsson, M. & Perrimon, N. Understanding cellular signaling and systems biology with precision: a perspective from ultrastructure and organelle studies in the Drosophila midgut. *Curr. Opin. Syst. Biol.* **11**, 24–31 (2018).
18. Rodrigues, F. F. & Harris, T. J. C. Key roles of Arf small G proteins and biosynthetic trafficking for animal development. *Small GTPases* **10**, 403–410 (2019).
19. Tsarouhas, V. et al. Sequential pulses of apical epithelial secretion and endocytosis drive airway maturation in Drosophila. *Dev. Cell* **13**, 214–225 (2007).
20. Wilfling, F. et al. Arf1/COPI machinery acts directly on lipid droplets and enables their connection to the ER for protein targeting. *Elife* **3**, e01607 (2014).
21. Jayaram, S. A. et al. COPI vesicle transport is a common requirement for tube expansion in Drosophila. *PLoS ONE* **3**, e1964 (2008).
22. Parkinson, W. M. et al. Synaptic roles for phosphomannomutase type 2 in a new Drosophila congenital disorder of glycosylation disease model. *Dis. Model. Mech.* **9**, 513–527 (2016).
23. Ladyzhets, S. et al. Self-limiting stem-cell niche signaling through degradation of a stem-cell receptor. *PLoS Biol.* **18**, e3001003 (2020).
24. Koehler, C. L., Perkins, G. A., Ellisman, M. H. & Jones, D. L. Pink1 and Parkin regulate Drosophila intestinal stem cell proliferation during stress and aging. *J. Cell Biol.* **216**, 2315–2327 (2017).
25. Xu, C. et al. The septate junction protein Tsp2A restricts intestinal stem cell activity via endocytic regulation of aPKC and Hippo signaling. *Cell Rep.* **26**, 670–688.e6 (2019).
26. Corrigan, L. et al. BMP-regulated exosomes from Drosophila male reproductive glands reprogram female behavior. *J. Cell Biol.* **206**, 671–688 (2014).
27. Jumper, J. et al. Highly accurate protein structure prediction with AlphaFold. *Nature* **596**, 583–589 (2021).
28. Giovannini, D., Touhami, J., Charnet, P., Sitbon, M. & Battini, J. L. Inorganic phosphate export by the retrovirus receptor XPR1 in metazoans. *Cell Rep.* **3**, 1866–1873 (2013).
29. Ma, B. et al. A plasma membrane transporter coordinates phosphate reallocation and grain filling in cereals. *Nat. Genet.* **53**, 906–915 (2021).
30. Balis, J. U. & Conen, P. E. The Role of Alveolar Inclusion Bodies in the Developing Lung. *Lab. Invest.* **13**, 1215–1229 (1964).
31. Suzuki, H. & Kurosumi, K. Lamellar granules and keratohyalin granules in the epidermal keratinocytes, with special reference to their origin, fate and function. *J. Electron Microsc. (Tokyo)* **21**, 285–292 (1972).
32. Osanai, K. et al. Pulmonary surfactant transport in alveolar type II cells. *Respirology* **11** (Suppl. 1), S70–S73 (2006).
33. Tarutani, M. et al. GPHR-dependent functions of the Golgi apparatus are essential for the formation of lamellar granules and the skin barrier. *J. Invest. Dermatol.* **132**, 2019–2025 (2012).
34. Schmitz, G. & Muller, G. Structure and function of lamellar bodies, lipid-protein complexes involved in storage and secretion of cellular lipids. *J. Lipid Res.* **32**, 1539–1570 (1991).
35. Dillard, K. J. et al. Recessive missense LAMP3 variant associated with defect in lamellar body biogenesis and fatal neonatal interstitial lung disease in dogs. *PLoS Genet.* **16**, e1008651 (2020).
36. Cheong, N. et al. ABCA3 is critical for lamellar body biogenesis in vivo. *J. Biol. Chem.* **282**, 23811–23817 (2007).
37. Gilder, H., Haschemeyer, R. H., Fairclough, G. F. Jr & Mynarcik, D. C. Isolation and characterization of lamellar body material from rat lung homogenates by continuous linear sucrose gradients. *J. Lipid Res.* **22**, 1277–1285 (1981).
38. Ridsdale, R., Na, C. L., Xu, Y., Greis, K. D. & Weaver, T. Comparative proteomic analysis of lung lamellar bodies and lysosome-related organelles. *PLoS ONE* **6**, e16482 (2011).
39. Wang, P. et al. Proteomic analysis of lamellar bodies isolated from rat lungs. *BMC Cell Biol.* **9**, 34 (2008).
40. Raymond, A. A. et al. Lamellar bodies of human epidermis: proteomics characterization by high throughput mass spectrometry and possible involvement of CLIP-170 in their trafficking/secretion. *Mol. Cell Proteomics* **7**, 2151–2175 (2008).
41. Chintagari, N. R. et al. Effect of cholesterol depletion on exocytosis of alveolar type II cells. *Am. J. Respir. Cell Mol. Biol.* **34**, 677–687 (2006).
42. Carvalho, M. et al. Effects of diet and development on the Drosophila lipidome. *Mol. Syst. Biol.* **8**, 600 (2012).
43. Guan, X. L. et al. Biochemical membrane lipidomics during Drosophila development. *Dev. Cell* **24**, 98–111 (2013).
44. Grayson, S. et al. Lamellar body-enriched fractions from neonatal mice: preparative techniques and partial characterization. *J. Invest. Dermatol.* **85**, 289–294 (1985).
45. Giot, L. et al. A protein interaction map of Drosophila melanogaster. *Science* **302**, 1727–1736 (2003).
46. Jiang, H. et al. Cytokine/Jak/Stat signaling mediates regeneration and homeostasis in the Drosophila midgut. *Cell* **137**, 1343–1355 (2009).
47. Martin-Blanco, E. et al. *puckered* encodes a phosphatase that mediates a feedback loop regulating JNK activity during dorsal closure in *Drosophila*. *Genes Dev.* **12**, 557–570 (1998).
48. Patel, P. H. et al. Damage sensing by a Nox-Ask1-MKK3-p38 signaling pathway mediates regeneration in the adult Drosophila midgut. *Nat. Commun.* **10**, 4365 (2019).
49. Eichhorn, P. J., Creyghton, M. P., Wilhelmsen, K., van Dam, H. & Bernards, R. A RNA interference screen identifies the protein phosphatase 2A subunit PR55gamma as a stress-sensitive inhibitor of c-SRC. *PLoS Genet.* **3**, e218 (2007).
50. Michigami, T., Kawai, M., Yamazaki, M. & Ozono, K. Phosphate as a signaling molecule and its sensing mechanism. *Physiol. Rev.* **98**, 2317–2348 (2018).

Article

Methods

Drosophila stocks

The following strains were obtained from the Bloomington *Drosophila* Stock Center (BDSC): *y v;attP2* (*Ctrl^b*, landing site only, BL36303), *UAS-Luc-i* (BL31603), *UAS-PXo-i* (BL34551), *UAS-p35* (BL5073; ref. 51), *nos-Cas9/CyO* (BL78781), *esg-lacZ* (BL10359), *hsp70-Mos1-Cre* (BL1092), *20×UAS-6×GFP* (BL52261), *PXo^PL48 FRT2A FRT82B* (BL19366), *FRT2A FRT82B* (BL8218), *hsp70-piggyBac* (BL8284), *UAS-RFP-KDEL* (BL30910), *UAS-ManII-TagRFP* (BL65249), *UAS-GalT-TagRFP* (BL65251), *UAS-Sar1-i* (BL32364; ref. 52), *UAS-Arf1-i* (BL66174; ref. 53), *UAS-γCOP-i* (BL28890), *UAS-Pmm2-i* (BL42956), *UAS-Pink1-i* (BL31170), *UAS-Parkin-i* (BL37509), *UAS-Lamp1-i* (BL38335), *UAS-ABCA-i^1* (BL38329; ref. 54), *UAS-ABCA-i^2* (BL38353; ref. 55), *UAS-Rab7-i* (BL27051), *UAS-Rab11-i^1* (BL27730), *UAS-Rab11-i^2* (BL42709), *UAS-GFP-LAMP1* (BL42714), *UAS-Atg8a-GFP* (BL52005), *UAS-Tsp2A-i* (BL40899), *UAS-hts-mCherry* (BL66171), *UAS-SERCA-tdTomato* (BL58971), *UAS-Ogdh-Flag* (BL77505), *UAS-Idh-Flag* (BL56201), *Idh3a-GFP* (BL82434), *Treh-GFP* (BL59825), *Ance-GFP* (BL59828), *UAS-Mipp1-GFP* (BL78062), *UAS-Cka-i* (BL28927), *UAS-Mob4-i* (BL65236), *UAS-Mob4-i^2* (BL36488), *UAS-bsk-i* (BL31323), *UAS-Strip-i* (BL34657), *UAS-mts-i* (BL38337) and *UAS-Pp2A-29B-i* (BL29384). Stocks from the Vienna *Drosophila* RNAi Center (VDRC, with superscript label 'v') were as follows: *y w;attP* (*Ctrl^v*, landing site only, v60100), *UAS-PXo-i^v* (v100151), *UAS-MFS10-i^v* (v108045), *UAS-Cka-i^v* (v35234), *UAS-Mob4-i^v* (v40442) and *UAS-Strip-i^v* (v16211). Stocks from the National Institute of Genetics (NIG, with superscript label 'N') were as follows: *UAS-PXo-i^N* (10483R-3). *EGT;UAS-Flp, Act>Stop>Gal4* (EGT F/O[56]) was from B. Edgar (the University of Utah). *UAS-H2B-RFP* was from N. Buchon (Cornell University). *tubGal80^ts;DlGal4* (*DlGal4^ts*) and *tubGal80^ts;Su(H)Gal4* (*Su(H)^ts*) were from S. Hou (NIH). *UAS-CD63-GFP* was from C. Wilson (Oxford University). *UAS-Vha55-GFP* was from F. Pignoni (Upstate Medical University). *tub-Flag-Cka* was from D. Pan (UT Southwestern Medical Center). *UAS-BFP-Cka* was from T. Hays (University of Minnesota). The fly stock for MARCM analysis, *yw hs-FLP tub-GAL4 UAS-nls-GFP;FRT2A tub-GAL80*, was from H. Jiang (UT Southwestern Medical Center). Stocks from the Perrimon laboratory were as follows: *w1118*, *Ore^R*, *UAS-GFP*, *esgGFP*, *tubGal80^ts;Myo1AGal4* (*Myo1A^ts*), *tubGal80^ts;tubGal4* (*tub^ts*), *esgGal4 UAS-GFP tubGal80^ts* (*EGT*), *tubGal80^ts;esgGal4* (*esg^ts*), *tubGal80^ts;DaGal4* (*Da^ts*), *tubGal80^ts;ProsGal4* (*ProsGal4^ts*, made with *ProsGal4* from A. Bardin (Institut Curie)), *PXoGal4* and *PXo^2xHA*. The following stocks were generated in this study: *PXoGal4*, *PXo^rev FRT2A FRT82B*, *UAS-GFP-PXo*, *UAS-GFP-PXo^△SPX*, *PXo^2×HA*, *UAS-PXo-HA* and *UAS-FLIPPi*. A complete list of fly genotypes used in this study is presented in Supplementary Table 4.

PXo^rev FRT2A FRT82B was generated by crossing *PXo^PL48 FRT2A FRT82B* to flies that express the piggyBac transposase (*hsp70-piggyBac*)[57]. Because the transposon carries the eye-specific 3×P3–EYFP fluorescent marker, the loss of eye fluorescence was used to screen for revertant flies. Note that, whereas *PXo^PL48* is homozygous lethal, *PXo^rev* is homozygous viable.

The sequence-verified *PXo* cDNA coding sequence (CDS) was cloned from *GH26628* (*Drosophila* Genomics Resource Center, DGRC) into the pEntr/D-Topo vector (Invitrogen, K240020) and then into pTGW (using the CDS with a stop codon) or pTWH (using the CDS without a stop codon) expression vectors (*Drosophila* Gateway Vector collection) with the Gateway LR Clonase II kit (Invitrogen, 11791020) to generate plasmids injected for *UAS-GFP-PXo* or *UAS-PXo-HA* transgenic flies. To generate *UAS-GFP-PXo^△SPX* transgenic flies for expression of a truncated version of PXo lacking the SPX domain (amino acids 1–193), the *UAS-GFP-PXo* plasmid was digested with SacII (NEB, R0157) and KpnI (NEB, R0142) and then circularized by Gibson assembly (NEB, E2611) to obtain the plasmid for injection. Red eye colour was used to screen for transgenic flies because the expression vectors carry the *w⁺* marker.

Sequence-verified *FLIPPi* was cloned from pLR364-cpFLIPPi-6.4 into pEntr/D-Topo with a pair of primers (5′-CACCGGTAGAAAAAGACCGGG-3′ and 5′-CGAATGCTAAGCTTTTACTCGATG-3′) and then into the pTW expression vector to generate the plasmid for *UAS-FLIPPi* transgenic flies. Red eye colour was used to screen for transgenic flies.

CRISPR–Cas-mediated genomic editing

PXoGal4 was generated by single guide RNA (sgRNA)–Cas9-mediated genome editing. We cloned the pCFD3-U6-PXo-sgRNA plasmid by inserting an sgRNA that targets the *PXo* translational start site (seed sequence, 5′-GCGAACTTCATCTCGGGAATTGG-3′) into the pCFD3 vector (Addgene, 49410) and generated a Gal4 version of the pHD-DsRed donor plasmid with ~1-kb sequence-verified homology arms on each end. After injection of a 1:1 mixture of sgRNA and donor plasmid in injection buffer (5 mM KCl and 100 μM sodium phosphate buffer, pH 6.8) into fly embryos expressing Cas9 (genotype, *nanos-Cas9/CyO*). The *loxP*-flanked sequence encoding the 3×P3–dsRed fluorescent marker in the donor vector was used to screen for knock-in flies in parental and F_1 generations and was subsequently removed by crossing to flies that expressed Cre recombinase (*hsp70-Mos1-Cre*). *PXoGal4* knock-in stocks were confirmed by genotyping PCR using two pairs of primers (forward and reverse): gtPCR1 (5′-GATGAAGCCCATGTCCAAGT-3′ and 5′-AGCGGAGACCTTTTGGTTTT-3′) and gtPCR2 (5′-CACAACCAATTGCCTCCTCT-3′ and 5′-GTGGGACTTCGACCAAAGAA-3′).

To obtain *PXo^2×HA* flies, we cloned the homology arm upstream of the endogenous *PXo* start codon with the primer pair of 5′-TTGTGCAGGCGACTCTTCGG-3′ and 5′-CTCGGGAATTGGGGGGATCTCACAAC-3′ and the downstream homology arm with the primer pair of 5′-ATGAAGTTCGCCGAGCACCT-3′ and 5′-CGATCTCCTCCCTCGATGTCC-3′. The two arms were inserted into the pScarlessHD-2×HA-DsRed vector (Addgene, 80822) by Gibson assembly to generate the donor plasmid pScarlessHD-PXo-N-2×HA-DsRed, which was subsequently mixed with the pCFD3-U6-PXo-sgRNA plasmid for injection into fly embryos expressing Cas9. The edited flies were selected by DsRed fluorescence, confirmed by genotyping PCR with the gtPCR3 (5′-CGAGAGGCGTTTTCATTTGT-3′ and 5′-CAGACCGATAAAACACATGCGTCA-3′) and gtPCR4 (5′-TCCTAAATGCACAGCGACGGATTCG-3′ and 5′-AGAGGCATTCGATGATGAGG-3′) primer pairs and crossed to flies expressing the piggyBac transposase to remove the DsRed cassette. The resulting *PXo^2×HA* flies were identified by the loss of DsRed fluorescence, genotyped with the gtPCR5 primer pair (5′-TGGCCCAGTTGTGATGTTTA-3′ and 5′-ATTTTCGGCACTCACCTCAT-3′) and verified by sequencing the genotyping PCR product.

Drosophila culture and drug treatment

Flies were reared on standard cornmeal/agar medium (fly food). We kept a consistent number of adult flies (usually ~15 females and 5 males) in each vial and replaced their food every other day to keep the vials clean. For conditional expression using *tubGal80^ts*, flies were kept at 18 °C until eclosion, maintained at 18 °C for an additional 3–5 days to allow post-eclosion midgut development and then shifted to 29 °C to induce expression. For cell loss assays, young adult flies with 2 days of induction of enterocyte-specific expression of H2B–RFP were shifted back and kept at 18 °C for 11 days, with the last 9 days on normal or PFA food. For MARCM[58] experiments, flies were maintained at 18 °C until 3–5 days after eclosion, heat shocked at 37 °C for 1 h and then maintained at 18 °C until dissection and analysis.

To induce midgut damage, fly food was melted and mixed with a final concentration of 25 μg ml⁻¹ bleomycin (Calbiochem, 203408). For P_i starvation, we dissolved PFA (Sigma-Aldrich, P6801) in water to make 180 mM stocks and mixed them with melted fly food at a final concentration of 20 mM. We used food with a slightly higher dose of 30 mM PFA to accelerate PXo body degradation (for observation with 2 days of feeding) in the rescue experiments (Fig. 4k–m), which included food mixed with PFA alone, PFA together with 10 mg ml⁻¹ CQ (Sigma-Aldrich, C6628) and PFA together with 20 μM MG132 (Calbiochem, 474791). The

concentrations of CQ and MG132 were based on previous characterization[59]. For additional P_i feeding, we prepared a concentrated stock of 900 mM Na_2HPO_4/NaH_2PO_4 (adjusted to pH 7) and mixed this with melted fly food at a 30 mM final concentration. Fly food containing the same concentration of Na_2SO_4 (pH 7) was included to control for changes in salt concentration in the P_i food. In addition to the sodium salts used throughout this study, we also made consistent observations with potassium salts. For additional phospholipid feeding, we mixed PC (Sigma-Aldrich, 1535733) with melted fly food at a 1% or 5% concentration by weight. We added the same amount of water to melted fly food to make normal food the control for drug stocks prepared in water solutions. Moreover, we weighed the food before and after melting to measure the volume of additional water required in each group to compensate for evaporation.

The S2R$^+$ cell line was obtained from the *Drosophila* RNAi Screening Center/Transgenic RNAi Project Functional Genomics Resources and *Drosophila* Research & Screening Center–Biomedical Technology Research Resource at Harvard Medical School. It has a distinct morphology that can be relied on for quality control in routine passaging. Moreover, it has been molecularly validated by transposable element DNA sequencing[60]. S2R$^+$ cells were cultured in Schneider's Insect Medium (Sigma-Aldrich, S0146) in a 25 °C tissue culture incubator. The *PXo* CDS (from DGRC *GH26628*) was cloned into the pAGW expression vector (*Drosophila* Gateway Vector collection), and the resulting vector was transfected into S2R$^+$ cells with Effectene transfection reagent (Qiagen, 301427). For drug treatment, transfected S2R$^+$ cells were seeded on cover slides in a culture dish and incubated with 30 mM PFA, 30 mM PFA together with 100 nM BafA1 or 30 mM PFA together with 20 μM MG132 for 24 h before fixation and staining.

Drosophila CDF

CDF was prepared as previously described[61] with slight modifications. First, we prepared the base buffer, which contained 30 g L^{-1} KH$_2$PO$_4$ (Sigma, P9791; dissolved in water unless noted otherwise), 10 g L^{-1} NaHCO$_3$ (Sigma, S8875) and 30 ml L^{-1} glacial acetic acid (Millipore, AX0074). For 20% P_i and 10% P_i CDF, 6 g L^{-1} and 3 g L^{-1} KH$_2$PO$_4$ were used, respectively, with an appropriate amount of K$_2$SO$_4$ (Sigma, P0772) added to maintain the potassium ion concentration. For isotopic P_i tracing, we used ^{18}O-labelled KH$_2$PO$_4$ (Cambridge Isotope Laboratories, OLM-7493-PK).

Second, we prepared the vitamin solution, which contained 0.1 g L^{-1} thiamine (Sigma, T4625), 0.05 g L^{-1} riboflavin (Sigma, R4500), 0.6 g L^{-1} nicotinic acid (Sigma, N4126), 0.775 g L^{-1} calcium pantothenate (Sigma, P21210), 0.125 g L^{-1} pyridoxine (Sigma, P9755) and 0.01 g L^{-1} biotin (Sigma, B4501). Third, we prepared the nutrient supplement, which contained 6.25 g L^{-1} choline chloride (MP Biomedicals, 194639), 0.63 g L^{-1} myo-inositol (Sigma, I7508), 8.13 g L^{-1} inosine (Sigma, I4125) and 7.5 g L^{-1} uridine (Sigma, U3003). For a final volume of 1 L of CDF, we prepared CDF-fraction A, which included 100 ml base buffer, 21 ml vitamin solution, 8 ml nutrient supplement, 10 ml of 163 g L^{-1} arginine HCl (Amresco, 0877), 10 ml of 34 g L^{-1} cysteine (Sigma, 30089; in 1 N HCl), 10 ml of 152 g L^{-1} glutamic acid monosodium salt monohydrate (Alfa Aesar, A12919), 10 ml of 77 g L^{-1} glycine (Alfa Aesar, A13816), 10 ml of 137 g L^{-1} lysine HCl (Amresco, 0437), 10 ml of 98 g L^{-1} proline (Sigma, P5607), 10 ml of 138 g L^{-1} serine (Sigma, S4311), 50 ml of 22 g L^{-1} alanine (Sigma, A7469), 50 ml of 20.6 g L^{-1} asparagine (Amresco, 94341), 50 ml of 23.4 g L^{-1} aspartic acid (Alfa Aesar, A13520; in 0.5 N NaOH), 50 ml of 22.4 g L^{-1} glutamine (Amresco, 0374), 50 ml of 40.6 g L^{-1} leucine (Sigma, L8912; dissolved in 0.2 N HCl), 50 ml of 6.4 g L^{-1} tryptophan (Amresco, E800), 1 ml of 0.5 g L^{-1} folic acid (Sigma, F8758; in 0.004 N NaOH), 6 ml propionic acid (Sigma, P5561) and 15 ml of 100 g L^{-1} methyl 4-hydroxybenzoate (Sigma, H3647; in 95% ethanol).

Next, for a final volume of 1 L of CDF, we prepared CDF-fraction B, which contained 50 ml of 13 g L^{-1} histidine stock solution (Amresco,

1B1164), 50 ml of 22.4 g L^{-1} isoleucine (Amresco, E803), 50 ml of 12 g L^{-1} methionine (Amresco, E801), 50 ml of 20.2 g L^{-1} phenylalanine (Sigma, P5482), 50 ml of 22.2 g L^{-1} threonine (Sigma, T8441), 50 ml of 24 g L^{-1} valine (Amresco, 1B1102), 0.93 g tyrosine (Sigma, T8566), 15 ml of 20 mg ml^{-1} cholesterol (Sigma, C8667; dissolved in ethanol), 1 ml of 250 g L^{-1} CaCl$_2$·6H$_2$O (Sigma, 21108), 1 ml of 2.5 g L^{-1} CuSO$_4$·5H$_2$O (Sigma, C7631), 1 ml of 25 g L^{-1} FeSO$_4$·7H$_2$O (Sigma, F7002), 1 ml of 250 g L^{-1} MgSO$_4$ (Sigma, M7506), 1 ml of 1 g L^{-1} MnCl$_2$·4H$_2$O (Sigma, M3634), 1 ml of 25 g L^{-1} ZnSO$_4$·7H$_2$O (Sigma, Z0251), 25 g sucrose (Sigma, S7903), 158 ml water (milliQ) and 10 g agar (Fisher Scientific, DF1040-07-4). CDF-fraction B was mixed well in a 1-L bottle with a magnetic stirrer and autoclaved at 120 °C for 15 min. After autoclaving, the hot CDF-fraction B was combined and mixed well with CDF-fraction A and aliquoted with ~5 ml per vial. After cooling and solidification, the CDF vials were covered with cotton plugs, covered with plastic wrap and stored at 4 °C for use within 1 month.

mRNA quantification

Total RNA was extracted from 15–20 midguts using TRIzol reagent (Thermo Fisher), treated with DNase I, purified using the Qiagen RNeasy kit and converted to cDNA using the iScript cDNA Synthesis kit (Bio-Rad). cDNAs were analysed by qPCR using the SYBR Green kit (Bio-Rad) and Bio-Rad CFX Manager software. *rp49* was used as the internal control (Fig. 1a). Both *GAPDH* and *rp49* were used as internal controls for other RT–qPCR experiments. Each RT–qPCR was performed with three technical replicates. Data from four biological replicates were quantified in Figs. 1d and 6d. Data from a representative biological replicate are presented in Extended Data Figs. 1e and 2b,c). qPCR primer pairs (forward and reverse) were as follows:

GAPDH: 5′-CCAATGTCTCCGTTGTGGA-3′ and 5′-TCGGTGTAGCCCACGGATT-3′;

rp49: 5′-ATCGGTTACGGATCGAACAA-3′ and 5′-GACAATCTCCTTGCGCTTCT-3′;

PXo_P1: 5′-CACCTGACGGCCCACATAAC-3′ and 5′-AGGGCGATTGTTCGATGGC-3′;

PXo_P2: 5′-CTTTGGTCGAAGTCCCACAT-3′ and 5′-GACCAGATGCGGAAATGACT-3′;

PXo_P3: 5′-AGTCATTTCCGCATCTGGTC-3′ and 5′-CATGTGTAGGCGTAGCAGGA-3′;

MFS10: 5′-GACGAACGGGAGGCGTTTT-3′ and 5′-AGGAAGCCCATGAATCCGAAA-3′;

Cka: 5′-TCAACGCTGGTGGACAGAAC-3′ and 5′-ATGCCCGGTATTGTGTATTGG-3′.

Anti-PXo antibody

Polyclonal anti-PXo antibody was generated by following an established protocol[62]. A short peptide (KKNKQEQRLLLQGESIEDLAS) was chosen as the antigen on the basis of predicted immunogenicity and specificity. The original cysteine residue in the C-terminal sequence of PXo (KKNKQEQRLLLQGESIEDLCS) was replaced with alanine because cysteine is prone to oxidation and erroneous downstream processing. The antigen was synthesized by GenScript, conjugated to keyhole limpet hemocyanin (KLH) and used to immunize rabbits for antibody production at Cocalico Biologicals (one initial inoculation followed by several booster injections). Serum was collected from immunized rabbits ~70–90 days after the initial inoculation.

Immunostaining and imaging analyses

Drosophila midguts (from female adults) or S2R$^+$ cells were fixed in 4% paraformaldehyde in PBS at room temperature for 1 h, incubated for 1–2 h in blocking buffer (5% normal donkey serum, 0.3% Triton X-100 and 0.1% BSA in PBS) and stained with primary antibodies overnight at 4 °C in PBST (0.3% Triton X-100 and 0.1% BSA in PBS). The primary antibodies and their dilutions were as follows: rabbit anti-pH3 (Millipore, 06-570; 1:3,000), mouse anti-GFP (Invitrogen, A11120; 1:300),

rabbit anti-GFP (Invitrogen, A6455; 1:500), rabbit anti-RFP (Life Technologies, R10367; 1:500), rabbit anti-β-galactosidase (Cappel, 0855976; 1:6,000), rabbit anti-Pdm1 (from X. Yang; 1:500), mouse anti-Pros (DSHB, MR1A; 1:50), mouse anti-HA (BioLegend, 901514 or Thermo Scientific, A-21287; 1:1,000), rat anti-HA (Sigma-Aldrich, 3F10; 1:1,000), rabbit anti-PXo (this study; 1:2,000), rabbit anti-cleaved caspase-3 (Cell Signaling, 9661; 1:500), goat anti-GMAP (DSHB, GMAP; 1:1,000), mouse anti-Cnx99A (DSHB, Cnx99A 6-2-1; 1:10), rabbit anti-Lgl (Santa Cruz, sc-98260; 1:300), mouse anti-ATP5A (Abcam, ab14748; 1:500), mouse anti-Hrs (DSHB, Hrs 27-4; 1:40), mouse anti-Rab7 (DSHB, Rab7; 1:40), rabbit anti-Lamp1 (Abcam, ab30687; 1:500), mouse anti-Dlg (DSHB, 4F3; 1:50), mouse anti-α-Spec (DSHB, 3A9; 1:50), rabbit anti-mCherry (Takara, 632496; 1:300), rabbit anti-Flag (Sigma-Aldrich, F7425; 1:2,000) and rabbit anti-phospho-p38 MAPK (Cell Signaling, 9211; 1:400). After incubation with primary antibody, the midguts or S2R$^+$ cells were washed three times with PBST, stained with DAPI (1:2,000 dilution) and Alexa Fluor-conjugated donkey anti-mouse, donkey anti-rabbit, donkey anti-goat or donkey anti-rat secondary antibodies (Molecular Probes/Invitrogen; 1:1,000) in PBST at 22 °C for 2 h, washed three times with PBST and mounted in Vectashield medium.

For mitosis quantification, the number of pH3$^+$ cells in the entire midgut was determined with an epifluorescence microscope. Unless noted otherwise, all images of the posterior midgut or S2R$^+$ cells that are presented in this study are confocal images acquired with a Zeiss LSM780 confocal microscope. A *z*-stack series of 10–20 images (or a higher number for thicker organs) covering one layer of the epithelium from the apical to the basal side were obtained, adjusted and assembled using NIH Fiji v.1.0 and are shown as a maximum projection unless noted otherwise. For MARCM analysis, we quantified ~15 clones per gut. For quantification of GFP-labelled PXo body density, we counted the PXo bodies and cells by applying the Fiji 'Process-Find Maxima' function to the GFP and DAPI channels, respectively. For quantification of GFP-labelled PXo body size (Fig. 4i), we analysed the GFP channel with the Fiji macro 'PXo_body_area' and plotted the normalized PXo body area with R Studio v.1.1.463 using our customized code 'PXo_size_violin'. A *z*-stack series of confocal images was analysed with Imaris software (x64 v.9.5.1) for 3D visualization (Fig. 2a,e–k and Extended Data Fig. 3h–r), Mander's coefficient colocalization analysis (Extended Data Figs. 3s and 5c), surface rendering and shortest distance calculation were performed for quantification of the subcellular localization of PXo bodies in relation to other markers (Fig. 2l,m,o and Extended Data Fig. 3t). For quantification of immunogold labelling (Fig. 2d), gold particles were counted in the multilamellar structures (PXo bodies) or other areas and normalized to the size of the corresponding areas using NIH Fiji v.1.0. All quantification data except the violin plots were visualized with GraphPad Prism software v.9.4.0.

ApopTag cell death staining was performed with the ApopTag Red In Situ Apoptosis Detection kit (Millipore, S7165) as previously described[63]. Midguts were dissected in PBS and fixed in 4% paraformaldehyde at room temperature for 1 h, rinsed in PBS three times (5 min each) and rinsed in 75 μl per gut of equilibration buffer for 10 min. The midguts were then submerged in 55 μl per gut of reaction mix with working-strength terminal deoxynucleotidyl transferase (TdT) enzyme (ratio of 7:3). After incubation at 37 °C for 1 h, the TdT reaction mix was replaced with 1 ml stop/wash buffer (diluted 1:34 in dH$_2$O) followed by incubation for 10 min at room temperature. Samples were then washed three times in PBS and incubated in 65 μl per gut of anti-digoxigenin–rhodamine solution (diluted 31:34 in ApopTag kit blocking solution) in a dark and moist chamber at room temperature for 30 min, rinsed four times in PBS and mounted in Vectashield medium with DAPI.

LysoTracker staining in live tissue was performed as previously described[64]. Midguts were dissected in PBS, incubated in 0.5 μM LysoTracker-Red (DND-99; Invitrogen, L-7528) in PBS for 3 min, rinsed and then transferred to PBS on microscope slides and photographed immediately.

For lipid staining, midguts were fixed in 4% paraformaldehyde in PBS at room temperature for 30 min, washed three times with PBS, incubated for 15 min in 2 μg ml^{-1} Nile Red (Sigma-Aldrich, N3013) in PBS and mounted in Vectashield medium with DAPI.

Lectin staining was performed according to the instruction manual (EY Laboratories). Specifically, midguts with induced ubiquitous expression of GFP–PXo for 3 days were dissected and fixed in 4% paraformaldehyde for 1 h, rinsed and permeabilized with PBS containing 0.5% Triton X-100 for 1 h, rinsed with lectin staining buffer (LSB; 0.05 M Tris solution containing 0.15 M NaCl and 0.004 M CaCl$_2$, pH adjusted to 7.0–7.2), stained with LSB containing DAPI and ~100 μg ml^{-1} Texas Red-conjugated WGA (EY Laboratories, T-2101-2) or Texas Red-conjugated ConA (EY Laboratories, T-1104-5) in a moist chamber on an orbital shaker at room temperature for 1 h, rinsed with LSB three times and mounted in Vectashield medium.

Tracing of newly synthesized or internalized membranes

P-Cho staining was adapted from previous studies in mice[65]. Specifically, adult flies with induced ubiquitous expression of GFP–PXo for 3 days were injected in the abdomen with ~0.5 μl of 1 mg ml^{-1} P-Cho (Aobious, AOBT7378) in DMSO using the CellTram 4r Oil microinjector (Eppendorf). The glass injection needles (Sutter Instrument, Q100-70-7.5) were pulled to the desired thickness and opening diameter using program P0 on a micropipette puller (Sutter Instrument, P-2000). At different post-injection time points, the midguts were dissected and stained using the Click-&-Go Plus 594 Imaging kit (Click Chemistry Tools, 1319) following the manufacturer's protocol. In brief, the dissected midguts were fixed in 4% paraformaldehyde for 1 h, washed three times in PBS (5 min each), permeabilized in PBS containing 0.5% Triton X-100 for 15 min, incubated in the Click-&-Go Imaging kit reaction cocktail in a moist chamber on an orbital shaker at room temperature for 30 min, rinsed once in Click-&-Go Imaging kit wash buffer (Component E), rinsed once in PBS and mounted in Vectashield medium with DAPI.

Dextran and avidin uptake assays (Fig. 2k,o and Extended Data Fig. 3r) were based on a previous description[66,67]. In brief, dissected midguts were incubated ex vivo with 2 mg ml^{-1} Texas Red-conjugated 10-kDa dextran (Invitrogen, D1828) or 80 μg ml^{-1} Texas Red-conjugated avidin (Thermo Fisher Scientific, A820) diluted in Schneider's medium (Thermo Fisher Scientific, 21720-024) at room temperature for 30 min, rinsed three times in PBS, fixed in 4% paraformaldehyde and stained following a standard protocol. In addition to the established protocols of ex vivo incubation, we also tried an alternative delivery approach in which flies were fed 5% sucrose solution containing 2 mg ml^{-1} Texas Red-conjugated dextran or 80 μg ml^{-1} Texas Red-conjugated avidin for 1 h, with consistent observations (Extended Data Fig. 3t).

Protein structure prediction and analysis

The predicted protein structures of *Drosophila* PXo (UniProt, Q9VRR2), human XPR1 (UniProt, Q9UBH6) and rice PHO1-2 (UniProt, Q6K991) can be found in the AlphaFold Protein Structure Database[68] and were visualized with its 3D viewer (http://alphafold.ebi.ac.uk). The prediction model and data are authorized for use in publications under a CC-BY-4.0 licence. We downloaded their corresponding Protein Data Bank (PDB) files and conducted pairwise structure alignment with 'jFATCAT (rigid)' parameters[69] on the RCSB PDB server (http://www.rcsb.org/alignment).

PXo body extraction, density gradient ultracentrifugation fractionation and purification

Following induced GFP–PXo labelling at 29 °C for 4 days, 20 adult midguts (genotype *tubGal4^{ts} UAS-GFP-PXo*) per group were dissected and placed in Eppendorf tubes containing 100 μl freshly prepared extraction buffer (2× protease and phosphatase inhibitors (Pierce, 78440) and 2 mM trypsin inhibitor benzamidine (Sigma-Aldrich, 434760) in 1× PBS). After briefly breaking up the midguts with Kimble Kontes pellet pestles

(Millipore, Z359947), the lysate was transferred to a 1-ml tight-type Dounce homogenizer on ice. An additional 900 µl of extraction buffer was used to rinse the tube and transferred to the same homogenizer. After homogenization with ~25 strokes on ice, the homogenate was centrifuged at 500*g* for 3 min at 4 °C, filtered through a 40-µm cell strainer (Falcon) to remove the cell debris and intact cells, and then used for density gradient ultracentrifugation or PXo body purification.

To measure the density of PXo bodies, we prepared iodixanol fractions by diluting OptiPrep (Sigma, D1556; 60% iodixanol) with extraction buffer to the following concentrations: 36%, 20%, 10% and 5%. Then, 200 µl of midgut homogenate was mixed with 1 ml of 36% iodixanol at the bottom of a 5-ml centrifugation tube (Bechman, 344057), resulting in a final concentration of 30% iodixanol. One millilitre each of the 20%, 10% and 5% fractions were gently and sequentially placed on top of the heavier fractions. The step gradient was then centrifuged in a swing-bucket rotor (Beckman, MLS-50) at 200,000*g* for 3 h at 4 °C and manually separated by slowly aspirating from the top of the tube with a pipette into ~300-µl fractions. Twenty microlitres of liquid per fraction was spread on a microscope slide and imaged under an epifluorescence microscope to identify the fractions most enriched for PXo bodies (Extended Data Fig. 9b–e). The refraction index (RI) of each fraction was measured on an Accurate analogue Abbe refractometer (A.KRÜSS, AR4). The density of each fraction was acquired by looking up the data table in OptiPrep Application Sheet C01. For calibration, we measured the RI of the 10–30% iodixanol solutions diluted with extraction buffer (Extended Data Fig. 9f). Approximately 100 µl of liquid per fraction was used for western blot analysis. Additionally, 100 µl of fraction 9 and 100 µl of fraction 10 were combined, incubated with regular EM fixative and subjected to EM analysis.

To purify PXo bodies, we adapted a previously established immunoprecipitation protocol for tagged lysosomes[70]. In brief, the filtered homogenate was centrifugated at 3,000*g* for 5 min at 4 °C. Afterwards, the supernatant was discarded, whereas PXo bodies at the bottom and sides of the tubes were rinsed and resuspended with 500 µl extraction buffer and transferred to a new tube. The steps of centrifugation and rinsing were repeated three times to enrich for PXo bodies and to remove GFP–PXo that was not assembled into PXo bodies. Then, 25 µl of Chromotek-GFP-Trap agarose beads (Bulldog Biotechnology, gta-20) were added to the final round of resuspended homogenate. After 5 h of incubation on a rotator at 4 °C, we precipitated the beads, discarded the supernatant and washed three times with extraction buffer. Finally, the PXo body-bound beads were resuspended in ~20 µl of extraction buffer and subjected to in-gel staining, proteomic analysis or lipidomic analysis. For in-gel staining, a small aliquot of melted 2% low-melting-point agarose (Invitrogen, 16520100) was mixed in a 55 °C heat block with an equal volume of rinsed homogenate (input), supernatant after Chromotek-GFP-Trap incubation or PXo body-bound beads. The resulting mixture was quickly spread on a microscope slide, solidified with cooling, encircled with a PAP pen, fixed with 4% paraformaldehyde for 30 min and stained in a humidified chamber.

Western blot analysis and co-immunoprecipitation
PXo is predicted to be highly hydrophobic. In our pilot experiments using conventional methods of sample boiling (data not shown), immunoblot signals for GFP- or Flag-tagged PXo (whether tagging was N or C terminal) were stuck around the loading position and failed to migrate down the protein gel, suggesting that PXo might form large aggregates at the boiling temperature. Through optimization of the sample preparation protocol, we found that incubation at 37 °C for at least 1 h, instead of boiling, ensured that PXo stayed soluble.

For western blot analysis with the anti-PXo antibody, pAGW-PXo or pAWH-GFP (with GFP cloned into the pAWH expression vector) was transfected into S2R+ cells and cells were incubated for 3 days and lysed with lysis buffer (Pierce, 87788) containing 2× protease and phosphatase inhibitors (Pierce, 78440). Lysates were incubated in 2× SDS sample

buffer (Thermo Scientific, 39001) containing 5% 2-mercaptoethanol at 37 °C for 1 h, run on a 4–20% polyacrylamide gel (Bio-Rad, 4561096) and transferred to an Immobilon-P polyvinylidene fluoride (PVDF) membrane (Millipore, IPVH00010). The membrane was blocked with 5% BSA in 1× Tris-buffered saline (TBS) containing 0.1% Tween-20 (TBST) at room temperature for 1 h, probed with rabbit anti-PXo antibody (this study; 1:5,000) or mouse anti-tubulin (Sigma-Aldrich, T5168; 1:5,000) overnight at 4 °C in 1× TBST with 5% BSA, washed with TBST and probed with horseradish peroxidase (HRP)-conjugated secondary antibody. The HRP signal was detected with enhanced chemiluminescence reagents (Amersham, RPN2209; Pierce, 34095).

For GFP–PXo, GFP–PXo$^{\triangle SPX}$ and tub-Flag–Cka western blots (Figs. 4m and 6e and Extended Data Fig. 7q), midguts from three adult females per group were dissected in PBS, placed in 100 µl lysis buffer (Pierce, 87788) with 2× protease and phosphatase inhibitors (Pierce, 78440) and 2 mM benzamidine (Sigma-Aldrich, 434760), and homogenized using Kimble Kontes pellet pestles (Millipore, Z359947). The protein lysates were incubated in 2× SDS sample buffer containing 5% 2-mercaptoethanol at 37 °C for at least 1 h and processed for western blot analysis as described above, with rabbit anti-GFP (Invitrogen, A6455; 1:10,000), mouse anti-Flag (Sigma, F3040; 1:5,000), rabbit anti-GAPDH (GeneTex, GTX100118; 1:10,000) or mouse anti-tubulin (Sigma, T5168; 1:5,000) as the primary antibody. The blots were imaged with ChemiDoc MP (Bio-Rad, 17001402), and the total signal intensity of each band was measured with NIH Fiji v.1.0 for quantification of relative expression normalized to the internal control of GAPDH or tubulin.

For western blot analysis of the midgut homogenate after density gradient ultracentrifugation, each fraction was incubated in 2× SDS sample buffer containing 5% 2-mercaptoethanol at 37 °C for at least 1 h and processed for western blot analysis as described above, with 5 µl of sample loaded on the gel for each fraction and rabbit anti-GFP (Invitrogen, A6455; 1:10,000) or mouse anti-ATP5a (Abcam, ab14748; 1:1,000) antibody used as the primary antibody.

For co-immunoprecipitation experiments, the CDSs for PXo, Cka (from DGRC *LD41760*) and Pp2A-29B (from DGRC *LD41760*) were cloned into the pEntr/D-Topo vector and then the pAGW or pAFW expression vector (*Drosophila* Gateway Vector collection). Note that, although Cka and Pp2A-29B have multiple annotated isoforms, *LD41760* and *LD41760* harbour the CDSs for isoforms predicted to be the ones prominently expressed in the midgut, that is, Cka-RA/RB/RC/RD and Pp2A-29B-RA/RB/RC. We sequence verified the clones and corrected a C/– mutation in the *Pp2A-29B* CDS found at position 1229 of *LD41760*. Mixtures of expression plasmids or the negative control of pAWH-GFP was transfected into S2R+ cells in a 10-cm plate. After 3 days of incubation, cells were lysed with lysis buffer (Pierce, 87788) with 2× protease and phosphatase inhibitors (Pierce, 78440). Lysate was incubated with Chromotek-GFP-Trap beads (Bulldog Biotechnology, gta-20) for at least 2 h at 4 °C to precipitate protein complexes. Beads were washed 3–4 times with 1 ml lysis buffer and incubated in 2× SDS sample buffer containing 5% 2-mercaptoethanol at 37 °C for at least 1 h. The eluted samples were loaded on a 4–20% polyacrylamide gel for western blot analysis. We used rabbit anti-GFP (Invitrogen, A6455; 1:10,000) or mouse anti-Flag (Sigma-Aldrich, F3165; 1:5,000) antibody as the primary antibody.

Proteomic and lipidomic analyses of purified PXo bodies
In addition to the GFP–PXo-labelled experimental groups, we included Chromotek-GFP-Trap immunoprecipitation of midguts expressing GFP (genotype *tubGal4^{ts} UAS-GFP*) as a negative control. For proteomic analysis with LC–MS/MS, the resuspended PXo body-bound or GFP-bound Chromotek-GFP-Trap beads were mixed well with a final concentration of 2× SDS sample buffer and 5% 2-mercaptoethanol, incubated at 37 °C for at least 1 h and loaded on a 4–20% polyacrylamide gel. The gel was stained with Coomassie brilliant blue (Bio-Rad) and cut in small pieces for in-gel trypsin digestion, with resulting samples subjected

Article

to label-free quantitative MS with a high-resolution Thermo QExactive HF Orbitrap mass spectrometer. Proteins and tryptic peptides were identified using the Mascot 2.7 search engine relative to the *Drosophila* protein database (UniProt) followed by analysis with Scaffold Q+S 5.1 software (Proteome Software). GO analysis was performed using DAVID (https://david.ncifcrf.gov/)[71,72]. DIOPT Ortholog Finder (https://www.flyrnai.org/cgi-bin/DRSC_orthologs.pl) was used to identify the mammalian orthologues for *Drosophila* proteins[73].

The lipidomics analysis was performed as previously described[74]. In brief, 20 µl of the resuspended PXo body-bound or GFP-bound beads was mixed with 150 µl of HPLC-grade methanol and vortexed for 1 min. Then, 500 µl MTBE (methyl *tert*-butyl ether; Sigma-Aldrich, 34875) was added, and the mixture was incubated in a shaker at room temperature for 1 h, followed by addition of 120 µl water and vortexing for 1 min. The mixture was then centrifuged at 1,000*g* for 10 min at room temperature, after which we collected the upper MTBE liquid phase containing the non-polar lipids, mixed the lower liquid phase with 2 volume parts of MTBE/methanol/water (with a volume ratio of 10:3:2.5) and repeated centrifugation at 1,000*g* for 10 min to re-extract other lipids in the upper MTBE liquid phase. The combined MTBE phases were dried in a SpeedVac and analysed with untargeted high-resolution LC–MS/MS on a Thermo QExactive Plus Orbitrap mass spectrometer. LipidSearch v.4.2 (Thermo Scientific) was used to identify lipid molecules, with quantification of ion intensity by measuring the area of the identified peaks.

The ^{18}O isotopic lipidomic tracing of purified PXo bodies followed the same procedures for lipid extraction and LC–MS/MS as described above. The data were analysed with a modified version of the IsoSearch protocol[75]. In brief, the RAW files of unlabelled samples were processed with Scaffold Elements (Proteome Software; https://proteomesoftware.com/) and LipidSearch to obtain the pooled reference peak list with lipid *m/z* and RT information. All RAW files were converted to mzXML format using the 'Peak Picking' filter with MSConvertGUI (https://proteowizard.sourceforge.io/) and processed with the R package enviPick (https://rdrr.io/cran/enviPick/) to create MS[1] peak lists. We used the following enviPick parameters: MSlevel = c(1), dmzgap = 41; dmzdens = 20, drtgap = 300, drtsmall = 20, drtdens = 60, drtfill = 10, drttotal = 300, minpeak = 3, recurs = 3, weight = 1, SB = 1, SN = 3, minint = 1×10^3, maxint = 1×10^7, ended = 1 and ion_mode = positive/negative. The M peak lists were then compared against the pooled reference peak list using an in-house R programme IsoSearch. We used the following IsoSearch parameters: mass shift = 2.0042449933, rt_dist ≤ 2, mz_dist ≤ 10 and Score = 0.6.

Affinity purification LC–MS/MS analysis of PXo-interacting proteins

pAGW-PXo or pAWH-GFP (negative control) was transfected into S2R+ cells for 3 days of expression, after which the cells were lysed with lysis buffer (Pierce, 87788) with 2× protease and phosphatase inhibitors (Pierce, 78440). Lysate was incubated with Chromotek-GFP-Trap beads (Bulldog Biotechnology, gta-20) for at least 2 h at 4 °C to precipitate protein complexes. Beads were washed 3–4 times with 1 ml lysis buffer and incubated in 2× SDS sample buffer (Thermo Scientific, 39001) containing 5% 2-mercaptoethanol at 37 °C for at least 1 h. The eluted samples were loaded on a 4–20% polyacrylamide gel, digested in gel with trypsin and subjected to label-free quantitative MS/MS using a Thermo QExactive HF Orbitrap mass spectrometer. Proteins and tryptic peptides were identified using the Mascot search engine relative to the *Drosophila* protein database (UniProt). We performed complex enrichment analysis of the LC–MS/MS data using the protein Complex Enrichment Analysis Tool (COMPLEAT; https://www.flyrnai.org/compleat/)[76] with updated annotation for the STRIPAK complex[77] and intra-complex interactions (https://fgrtools.hms.harvard.edu/MIST/)[78]. For COMPLEAT analysis, the enrichment ratios were used as input values; the full list of protein-coding genes expressed in S2R+ cells[79] was used as the background.

Ultrastructural analysis

For EM, posterior midguts or midgut homogenate fractions were incubated in regular fixative (2.5% glutaraldehyde, 1.25% paraformaldehyde and 0.03% picric acid in 0.1 M sodium cacodylate buffer, pH 7.4) for at least 2 h at room temperature, washed in 0.1 M cacodylate buffer, post-fixed with 1% osmium tetroxide and 1.5% potassium ferrocyanide for 1 h, washed twice in water, washed once in maleate buffer (MB) and incubated in 1% uranyl acetate in MB for 1 h followed by two washes in water and dehydration in serial concentrations of ethanol (50%, 70%, 90%, 100%, 100%; 10 min each). The samples were then placed in propyleneoxide for 30 min and infiltrated overnight in a 1:1 mixture of propyleneoxide and TAAB epon (TAAB Laboratories Equipment). The following day, the samples were embedded in TAAB epon and polymerized at 60 °C for 48 h. Ultrathin plastic sections (~60 nm) were cut on a Reichert Ultracut-S microtome, picked up onto copper grids and contrasted with 0.3% lead citrate. Grids with the sections were imaged using a JEOL 1200-EX transmission electron microscope operating at 80 kV with an AMT 2k CCD camera. For quantification of unlabelled PXo body diameter, the long axis of oval-shaped multilamellar structures was measured with NIH Fiji v.1.0.

For EM with immunogold labelling, posterior midguts were fixed for 2 h in 0.1 M sodium phosphate buffer (pH 7.4) containing fresh 4% paraformaldehyde and 0.2% glutaraldehyde, rinsed in PBS and then either processed with osmium fixation and plastic embedding (as described for regular EM) or processed with 2.3 M sucrose cryoprotection and liquid nitrogen freezing. Plastic-embedded or frozen samples were cut into ~80-nm sections using a Reichert Ultracut S microtome and transferred to formvar-carbon-coated copper grids. Unless specified otherwise, staining was performed at 22 °C. Frozen sections were blocked in 1% BSA in PBS for 10 min, incubated with anti-GFP antibody (Abcam, 6556; 1:30 dilution) in 1% BSA in PBS for 1 h, washed four times in PBS, incubated with protein A-conjugated 15-nm gold particles (University Medical Center, Utrecht, the Netherlands) for 20 min, washed twice in PBS and four times in water, and incubated in a mixture of 0.3% uranyl acetate and 2% methyl cellulose for 5 min for contrast and embedding. Plastic sections were etched in saturated sodium *m*-periodate (Sigma-Aldrich, 71859) for 3 min, washed three times in water, blocked in PBT buffer (0.1% Triton X-100 and 1% BSA in PBS) for 30 min, incubated with rabbit anti-GFP (Abcam, 6556; 1:50 dilution) antibody in PBT buffer at 4 °C overnight, washed four times in PBS, incubated with protein A-conjugated gold particles for 20 min, washed twice in PBS and four times in water, and stained with lead citrate for contrast. Note that plastic sections preserve membrane morphology better, whereas frozen sections have improved labelling efficiency. For immunogold labelling with HIAR for the anti-PXo antibody, posterior midguts were fixed in 0.1 M sodium phosphate buffer (pH 7.4) containing fresh 4% paraformaldehyde for 2 h and processed with osmium fixation and plastic embedding. Approximately 80-nm ultrathin sections were picked up on uncoated 300 mesh nickel grids, etched in saturated sodium *m*-periodate for 5 min, washed three times in water, incubated with HIAR buffer (0.5 M Tris-HCl, pH 9.0) at 90 °C for 45 min, blocked in TBT buffer (0.1% Triton X-100 and 1% BSA in 10 mM Tris and 150 mM NaCl, pH 7.4) for 30 min, incubated with anti-PXo (this study; 1:50 dilution) antibody in TBT buffer at 4 °C overnight, washed four times in TBS (10 mM Tris and 150 mM NaCl, pH 7.4), incubated with protein A-conjugated gold particles for 30 min to 1 h, washed four times with TBS followed by three times with water, and stained with uranyl acetate and lead citrate for contrast. Grids with immunogold-labelled frozen or plastic sections were imaged the same way as for regular EM.

Live imaging for intracellular P$_i$ levels

Midguts from adult females expressing FLIPPi were dissected and handled in AHL buffer (2 mM CaCl$_2$, 5 mM KCl, 5 mM HEPES, 8.2 mM MgCl$_2$, 108 mM NaCl, 4 mM NaHCO$_3$, 1 mM NaH$_2$PO$_4$, 10 mM sucrose

and 5 mM trehalose, adjusted with NaOH to pH 7.5). One to two intact midguts were placed in single wells of eight-well clear-bottom cell culture chamber slides, gently oriented with nylon mesh on top, and immersed in 200 μl AHL buffer for imaging. FRET imaging and analysis were based on previously described intramolecular FRET protocols[80]. In brief, images or videos of the posterior midguts and blank regions were acquired on a wide-field fluorescence microscope (MicRoN Oscar) with a multiband dichroic and excitation filter for CFP/YFP (Chroma, 59217) and a Plan Fluor ×10/0.30-NA air DIC L/N1 objective. The acquisition parameters (that is, excitation filter and exposure time) were adjusted for each experiment to obtain optimal signal dynamic ranges and comparable signal intensity for the CFP and cpVenus (YFP) channels. For supplementation with additional P_i, we added 100 μl of freshly prepared AHL solution containing 90 mM Na_2HPO_4/NaH_2PO_4 (diluted from 900 mM, pH 7 stocks). In addition to sodium phosphate used in this study, we made consistent observations with potassium phosphate (K_2HPO_4/KH_2PO_4). FRET calculations were performed using Fiji with the 'Process-Image Calculator' function. We first subtracted from the CFP and YFP channels their corresponding blank signals (using images of blank regions acquired in the same experiment), extracted midgut regions that were in focus by image thresholding and divided the corrected cpVenus image by the corrected CFP image to obtain the image presenting FRET ratios in the midgut. For time-lapse analysis of average FRET ratios, we used the Fiji macro 'FRET_ratios_movie'.

Statistics and reproducibility

For western blots, imaging and RT–qPCR experiments, a representative result of three independent replicates is presented, unless the number of biological replicates is noted as being more than three. Statistical analyses were performed using GraphPad Prism. For comparison of any two data groups of different samples, P values were calculated by two-tailed Mann–Whitney U test. For comparison of multiple parallel data groups, P values were calculated by one-way ANOVA with Bonferroni's multiple-comparisons test. For comparison of two paired data groups using the same samples in EM (PXo immunogold labelling enrichment analysis) or P_i imaging (before and after P_i addition), P values were calculated by Wilcoxon signed-rank test. RT–qPCR data were analysed by two-tailed Welch's t-test. Single asterisk (*) indicates a P value that is greater than 0.01 but less than 0.05. Double asterisks (**) label a P value that is greater than 0.001 but less than 0.01. Triple asterisks (***) label a P value that is greater than 0.0001 but less than 0.001. Quadruple asterisks (****) label a P value that is less than 0.0001. P values of 0.05 or greater are labelled as 'not significant' (NS). No particular method was used to determine whether the data met the assumptions of the statistical approach. Sample sizes, determined empirically, are listed in the figure legends.

Schematics

Schematics were prepared using Office 365 (Microsoft) or BioRender. com with publication permissions.

Reporting summary

Further information on research design is available in the Nature Portfolio Reporting Summary linked to this article.

Data availability

All data supporting the findings of this study are available within the article and its Supplementary Information. Source data are provided with this paper.

Code availability

'PXo_body_area' is available at https://github.com/charles-xu-ru/image-analysis/blob/master/PXo_body_area. 'PXo_size_violin' is available at https://github.com/charles-xu-ru/image-analysis/blob/master/PXo_size_violin. 'FRET_ratios_movie' is available at https://github.com/charles-xu-ru/image-analysis/blob/master/FRET_ratios_movie.

51. Hay, B. A., Wolff, T. & Rubin, G. M. Expression of baculovirus P35 prevents cell death in Drosophila. *Development* **120**, 2121–2129 (1994).
52. Cook, M. S. et al. Neutral competition for Drosophila follicle and cyst stem cell niches requires vesicle trafficking genes. *Genetics* **206**, 1417–1428 (2017).
53. Lee, D. M., Rodrigues, F. F., Yu, C. G., Swan, M. & Harris, T. J. PH domain-Arf G protein interactions localize the Arf-GEF Steppke for cleavage furrow regulation in Drosophila. *PLoS ONE* **10**, e0142562 (2015).
54. Ueoka, I. et al. Novel genetic link between the ATP-binding cassette subfamily A gene and hippo gene in Drosophila. *Exp. Cell. Res.* **386**, 111733 (2020).
55. Moulton, M. J. et al. Neuronal ROS-induced glial lipid droplet formation is altered by loss of Alzheimer's disease-associated genes. *Proc. Natl Acad. Sci. USA* **118**, e2112095118 (2021).
56. Jiang, H. & Edgar, B. A. EGFR signaling regulates the proliferation of Drosophila adult midgut progenitors. *Development* **136**, 483–493 (2009).
57. Thibault, S. T. et al. A complementary transposon tool kit for Drosophila melanogaster using P and piggyBac. *Nat. Genet.* **36**, 283–287 (2004).
58. Wu, J. S. & Luo, L. A protocol for mosaic analysis with a repressible cell marker (MARCM) in Drosophila. *Nat. Protoc.* **1**, 2583–2589 (2006).
59. Tang, H. W. et al. The TORC1-regulated CPA complex rewires an RNA processing network to drive autophagy and metabolic reprogramming. *Cell. Metab.* **27**, 1040–1054.e8 (2018).
60. Mariyappa, D. et al. A novel transposable element-based authentication protocol for Drosophila cell lines. *G3 (Bethesda)* **12**, jkab403 (2022).
61. Piper, M. D. et al. A holidic medium for Drosophila melanogaster. *Nat. Methods* **11**, 100–105 (2014).
62. Field, C. M., Oegema, K., Zheng, Y., Mitchison, T. J. & Walczak, C. E. Purification of cytoskeletal proteins using peptide antibodies. *Methods Enzymol.* **298**, 525–541 (1998).
63. Ciesielski, H. M. et al. Erebosis, a new cell death mechanism during homeostatic turnover of gut enterocytes. *PLoS Biol.* **20**, e3001586 (2022).
64. Ren, C., Finkel, S. E. & Tower, J. Conditional inhibition of autophagy genes in adult Drosophila impairs immunity without compromising longevity. *Exp. Gerontol.* **44**, 228–235 (2009).
65. Jao, C. Y., Roth, M., Welti, R. & Salic, A. Metabolic labeling and direct imaging of choline phospholipids in vivo. *Proc. Natl Acad. Sci. USA* **106**, 15332–15337 (2009).
66. Wilcockson, S. G. & Ashe, H. L. Drosophila ovarian germline stem cell cytocensor projections dynamically receive and attenuate BMP signaling. *Dev. Cell* **50**, 296–312.e5 (2019).
67. Shravage, B. V., Hill, J. H., Powers, C. M., Wu, L. & Baehrecke, E. H. Atg6 is required for multiple vesicle trafficking pathways and hematopoiesis in Drosophila. *Development* **140**, 1321–1329 (2013).
68. Varadi, M. et al. AlphaFold Protein Structure Database: massively expanding the structural coverage of protein-sequence space with high-accuracy models. *Nucleic Acids Res.* **50**, D439–D444 (2022).
69. Li, Z., Jaroszewski, L., Iyer, M., Sedova, M. & Godzik, A. FATCAT 2.0: towards a better understanding of the structural diversity of proteins. *Nucleic Acids Res.* **48**, W60–W64 (2020).
70. Abu-Remaileh, M. et al. Lysosomal metabolomics reveals V-ATPase- and mTOR-dependent regulation of amino acid efflux from lysosomes. *Science* **358**, 807–813 (2017).
71. Huang da, W., Sherman, B. T. & Lempicki, R. A. Systematic and integrative analysis of large gene lists using DAVID bioinformatics resources. *Nat. Protoc.* **4**, 44–57 (2009).
72. Huang da, W., Sherman, B. T. & Lempicki, R. A. Bioinformatics enrichment tools: paths toward the comprehensive functional analysis of large gene lists. *Nucleic Acids Res.* **37**, 1–13 (2009).
73. Hu, Y. et al. An integrative approach to ortholog prediction for disease-focused and other functional studies. *BMC Bioinf.* **12**, 357 (2011).
74. Breitkopf, S. B. et al. A relative quantitative positive/negative ion switching method for untargeted lipidomics via high resolution LC-MS/MS from any biological source. *Metabolomics* **13**, 30 (2017).
75. Huang, H., Yuan, M., Seitzer, P., Ludwigsen, S. & Asara, J. M. IsoSearch: an untargeted and unbiased metabolite and lipid isotopomer tracing strategy from HR-LC-MS/MS datasets. *Methods Protoc.* **3**, 54 (2020).
76. Vinayagam, A. et al. Protein complex-based analysis framework for high-throughput data sets. *Sci. Signal.* **6**, rs5 (2013).
77. Neisch, A. L., Neufeld, T. P. & Hays, T. S. A STRIPAK complex mediates axonal transport of autophagosomes and dense core vesicles through PP2A regulation. *J. Cell Biol.* **216**, 441–461 (2017).
78. Hu, Y. et al. Molecular Interaction Search Tool (MIST): an integrated resource for mining gene and protein interaction data. *Nucleic Acids Res.* **46**, D567–D574 (2018).
79. Hu, Y., Comjean, A., Perrimon, N. & Mohr, S. E. The Drosophila Gene Expression Tool (DGET) for expression analyses. *BMC Bioinf.* **18**, 98 (2017).
80. Hodgson, L., Shen, F. & Hahn, K. Biosensors for characterizing the dynamics of rho family GTPases in living cells. *Curr. Protoc. Cell Biol.* https://doi.org/10.1002/0471143030.cb1411s46 (2010).

Article

Extended Data Fig. 1 | Related to Fig. 1. Characterization of Pi starvation and *PXo* knockdown. a,b, pH3 staining of midguts fed 7d normal or PFA food. **c,d**, pH3 staining of midguts fed 9d CDF containing standard (100%) or 10% Pi. **e**, RT-qPCR measurement of *MFS10* knockdown in the midgut when RNAi (VDRC line) is expressed 5d ubiquitously. The representative results with *n* = 3 technical replicates are presented. *P* = 0.0217. **f,g**, Midguts with 2d induced H2B-RFP expression in ECs, followed by 9d on normal or PFA food. **h,i,j,k**, Apoptag staining of midguts expressing *Luc* RNAi or *PXo* RNAi in ECs for 7d, with normal food (**h,k**), PFA, or the last 2d on Bleo. **l,m**, pH3 staining of midguts expressing *Luc* RNAi or *PXo* RNAi in ECs for 7d. **n,o**, pH3 staining and **r**, mitosis quantification of midguts with *PXo* RNAi (VDRC line) expression in ECs for 7d. *n* = 8 (Ctrl^w), 9 (PXo-i^v). *P* = 0.0193. **p,q**, pH3 staining of midguts expressing *Luc* RNAi or *PXo* RNAi in progenitors for 8d. **s**, Mitosis of midguts with *PXo* RNAi (NIG) expression in ECs for 9d. *n* = 12 (Ctrl^w), 15 (PXo-i^N). *P* = 7.94E-6. **t**, Mitosis of midguts expressing *Luc* RNAi or *PXo* RNAi alone, or together with p35 in progenitors for 9d, with or without the last 2d on Bleo. *n* = 14 (Luc-i Normal, Luc-i p35, PXo-i p35), 13 (PXo-i Normal, Luc-i Bleo, PXo-i Bleo). P values from left to right: 9.97E-8, 3.00E-3, 1.92E-7. **u**, Mitosis of midguts with or without *PXo* RNAi (NIG) expression in progenitors for 8d, fed normal food (*P* = 5.78E-5) or 2d Bleo (*P* = 0.0237). From left to right: N = 14, 13, 8, 12. **v**, Mitosis of midguts expressing GFP or p35 alone, or together with *PXo* RNAi in ECs for 9d. From left to right: *n* = 12, 10, 12, 14; *P* = 3.09E-6, 5.05E-3, 2.07E-7. **w**, Mitosis of midguts expressing *Luc* RNAi or *PXo* RNAi in progenitors, and fed normal, PFA, or Pi food for 7d. From left to right: *n* = 8, 9, 8, 7, 8, 9; *P* = 0.0132, 1.00, 1.40E-3, 1.18E-3, 1.00. **x**, Mitosis of midguts with or without *PXo-HA* expression in ECs for 8d, fed normal food or 2d Bleo. From left to right: *n* = 12, 12, 13, 13; *P* = 3.85E-7, 0.456, 3.85E-7. Data are mean ± s.e.m. *P* values are from two-tailed Welch's t test (**e**), two-tailed Mann-Whitney u test (**r,s,t,u,v,x**, between Luc-i and PXo-i Normal in **w**) or one-way ANOVA with Bonferroni's multiple comparison test (**w**). Arrowheads highlight pH3+ examples (**a–d,l–q**). Scale bars, 50 μm.
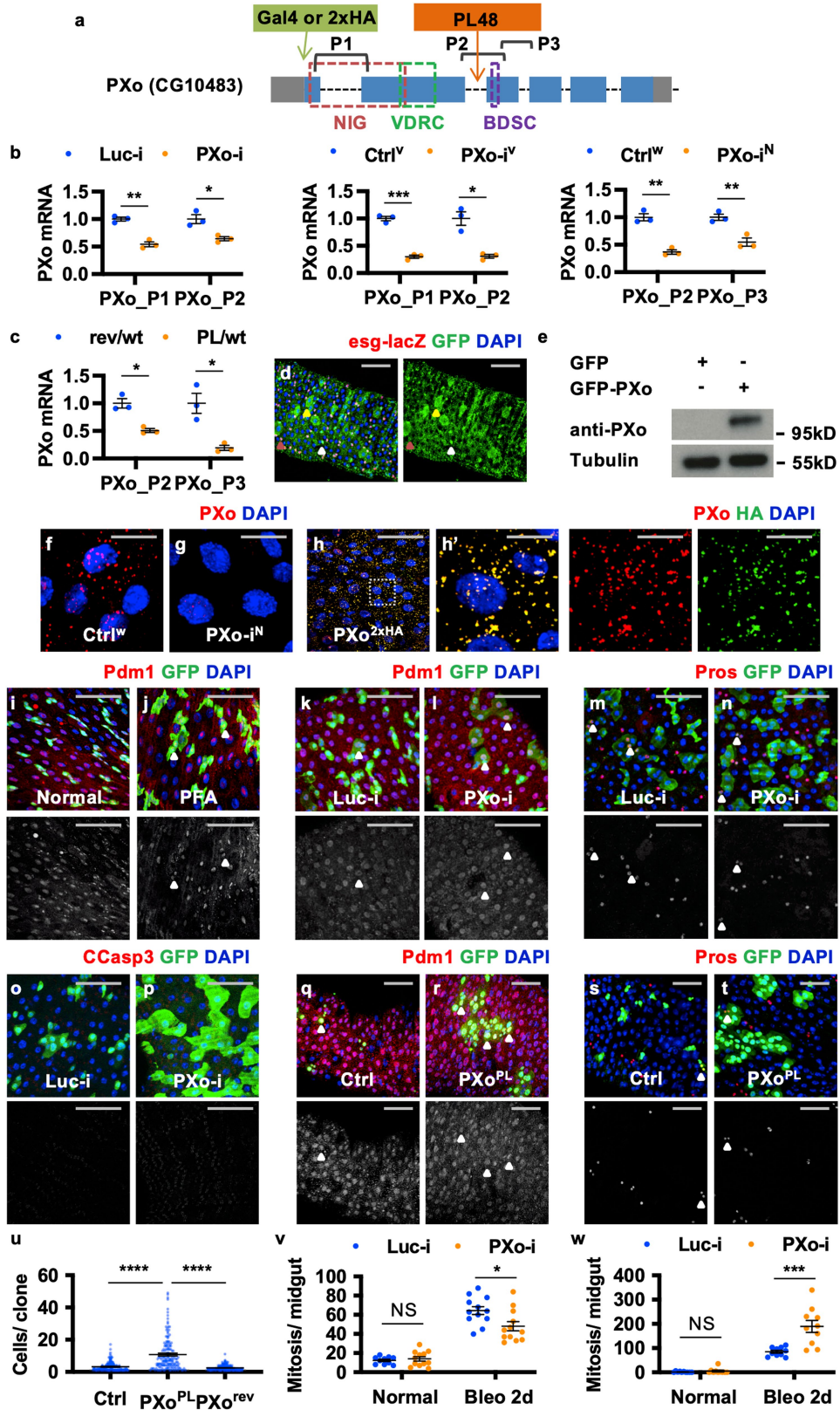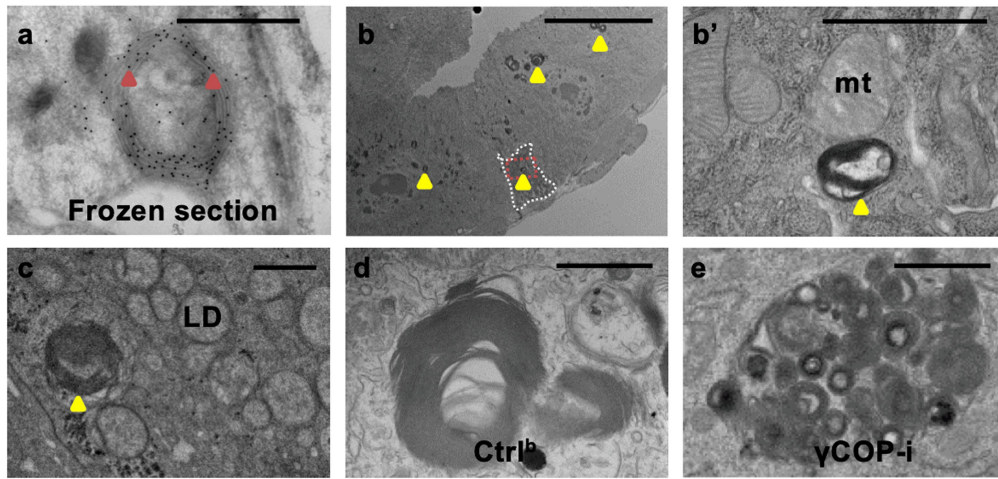
Extended Data Fig. 2 | See next page for caption.

Extended Data Fig. 2 | Related to Fig. 1. Characterization of *PXo* expression and phenotype in ISC/EB lineage. a, *PXo* genomic locus and target regions of reagents in this study, including 3 RNAi lines (from NIG, VDRC, or BDSC, as labeled by dashed squares) and 3 pairs of RT-qPCR primers (P1, P2, P3), a Gal4 knock-in allele, a 2xHA tag knock-in, and an insertional mutation (PL48). **b**, RT-qPCR measurement of *PXo* knockdown efficiency of three *PXo* RNAi lines expressed ubiquitously in the midgut for 5d. *Luc* RNAi was the control for *PXo* RNAi from BDSC, *Ctrl*^{w} was the control for *PXo* RNAi (VDRC), *Ctrl*^{w} was the control for *PXo* RNAi (NIG). The representative results with n = 3 technical replicates are presented. P values from left to right: 1.52E-3, 0.0305, 2.52E-4, 0.0236, 2.61E-3, 9.74E-3. **c**, RT-qPCR measurement of *PXo* expression in heterozygous midguts carrying one *PXo*^{PL48} mutant allele or its wild type revertant allele *PXo*^{rev}. The representative results with n = 3 technical replicates are presented. P values from left to right: 0.0162, 0.0405. **d**, *PXoGal4*-driven GFP co-staining with esg-lacZ. The single GFP channel is presented on the right. Red, yellow, white arrowheads mark examples of progenitor, EC, EE, respectively. **e**, Anti-PXo immunoblot of S2R$^+$ cell lysates expressing GFP or GFP-PXo. Tubulin was the loading control. Gel source data in Supplementary Fig. 1e. **f**,**g**, Anti-PXo staining of midguts with or without 5d ubiquitous *PXo* RNAi (NIG line) expression. **h**, Midguts with endogenous PXo tagged by 2 copies of HA epitope (*PXo*^{2xHA}) were co-stained with anti-HA and anti-PXo antibodies. A magnified view of the highlighted region is presented in (**h'**). The separate channels of PXo and HA stainings are shown on the right. **i**,**j**, Midguts expressing GFP in adult ISCs/EBs and their progenies (i.e. the ISC/EB lineage) were fed 10d normal food or PFA and stained for EC marker Pdm1. **k**,**l**,**m**,**n**,**o**,**p**, Midguts expressing *Luc* RNAi or *PXo* RNAi in the ISC/EB lineage (labeled by GFP expression) for 10d were stained for Pdm1, EE marker Pros, and apoptosis marker cleaved caspase 3 (CCasp3). **q**,**r**,**s**,**t**, Pdm1 or Pros staining of midguts with GFP$^+$ MARCM clones derived from wild type (n = 135 clones) or *PXo*^{PL48} mutant progenitors (n = 150) 10d after clone induction (dpi). Cell number per clone is quantified in (**u**). The *PXo*^{rev} allele generated by PBase-mediated precise excision of the inserted piggyBac transposon from mutant *PXo*^{PL48} allele was used as an additional control (n = 134). P < 1E-14 comparing *PXo*^{PL48} mutant versus Ctrl or *PXo*^{rev} wild type groups. **v**, Mitosis quantification of midguts expressing 8d *Luc* RNAi versus *PXo* RNAi in EEs, with normal food (P = 0.686) or 2d Bleo (P = 0.0179). n = 10 (Luc-i Normal), 12 (other groups). **w**, Mitosis of midguts expressing *Luc* RNAi or *PXo* RNAi in ISCs for 9d, with normal food (P = 0.771) or 2d Bleo (P = 6.50E-4). n = 10 per group. Data are mean ± s.e.m. P values are calculated from two-tailed Welch's t test (**b**,**c**) or two-tailed Mann-Whitney u test (**u**,**v**,**w**). The single red channels are presented in grayscale below merged images (**i–t**). White arrowheads highlight examples of traced cell differentiation. Scale bars, 50 μm (**d**,**h**,**i–t**), 10 μm (**f**,**g**,**h'**).
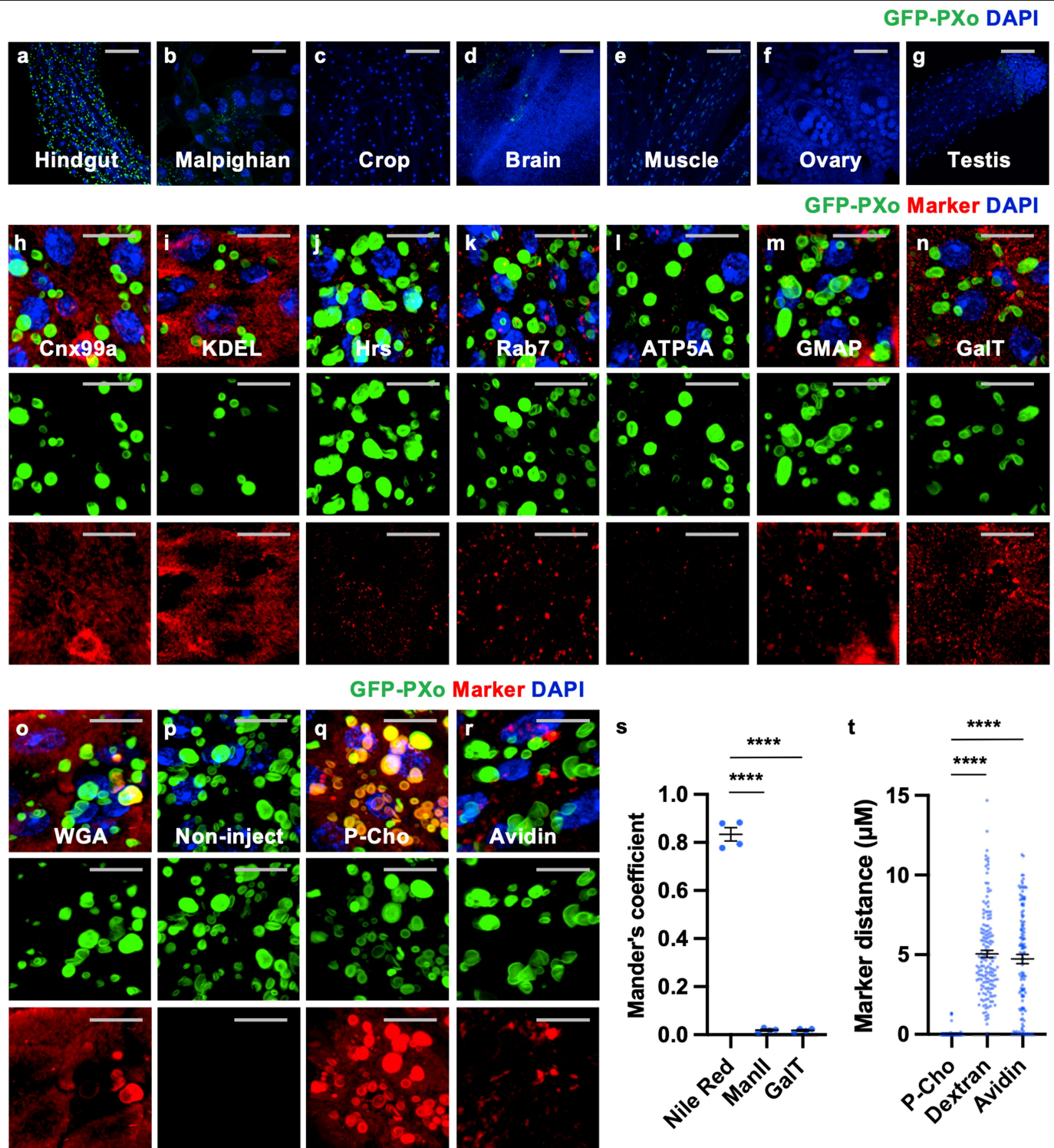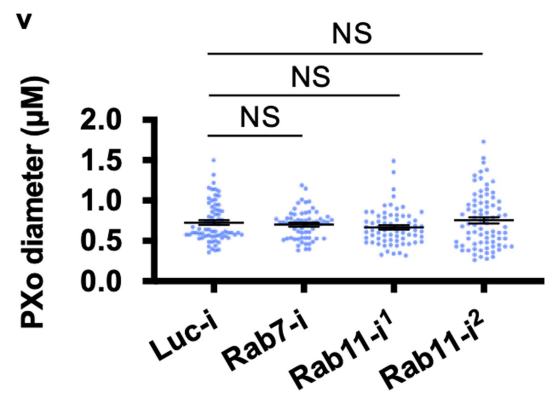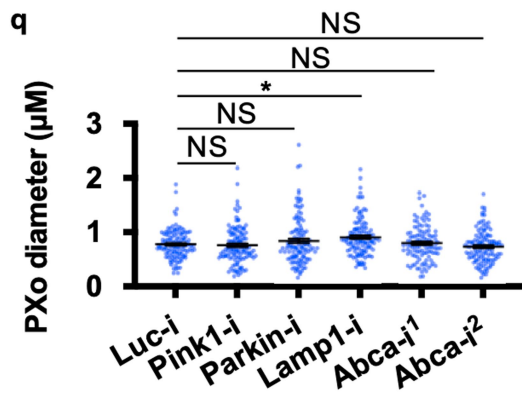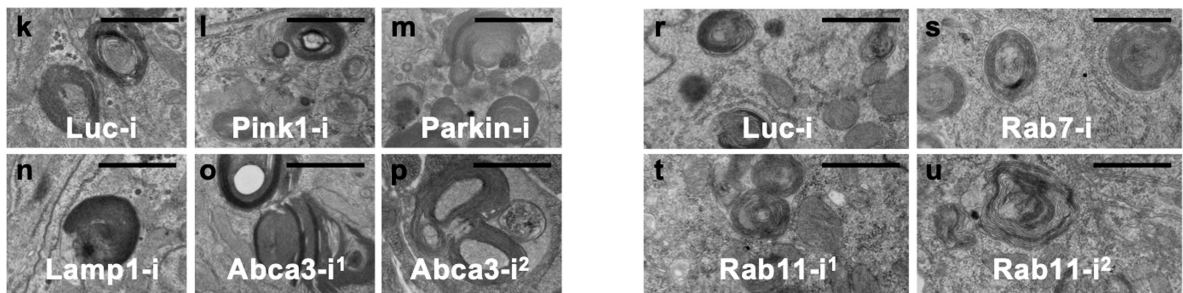
Extended Data Fig. 3 | Related to Fig. 2. Further analysis of PXo localization. **a**,**b**,**c**,**d**,**e**,**f**,**g**, GFP staining of different organs from adult flies with ubiquitous expression of GFP-PXo for 5d. **h**,**i**,**j**,**k**,**l**,**m**,**n**,**o**, Co-staining of ubiquitously expressed GFP-PXo with various markers in the midgut, including Cnx99a (ER), RFP-KDEL (ER lumen), Hrs (early endosome), Rab7 (late endosome), ATP5A (mitochondria), GMAP (cis-Golgi), GalT-TagRFP (trans-Golgi), and WGA (glycans). 3D view is presented. **p**,**q**, P-Cho staining of midguts with ubiquitously expression of GFP-PXo for 5d and collected 2h post P-Cho injection. A non-injection group was included as the negative control. 3D view of confocal image is presented. **r**, Co-staining of ubiquitously expressed GFP-PXo with Avidin (*ex vivo* incubation). 3D view of confocal image is presented. **s**, Co-localization analysis with the quantification of Mander's coefficient between GFP-PXo and Nile Red, ManII-TagRFP, or GalT-TagRFP. $n = 4$ midguts per group. P values from bottom to top: 1.16E-10, 1.14E-10. **t**, Shortest distance between each labeled PXo body and P-Cho (2h post injection), dextran (feeding), or avidin (feeding). $n = 185$ (P-Cho group), 149 (dextran), 122 (avidin) PXo bodies from 4 midguts were analyzed. $P < 1E-14$. Data are mean ± s.e.m. P values are from one-way ANOVA with Bonferroni's multiple comparison test (**s**, **t**). Separate green and red channels are presented below merged images (**h**–**r**). Scale bars, 50 μm (**a**–**g**), 10 μm (**h**–**r**).
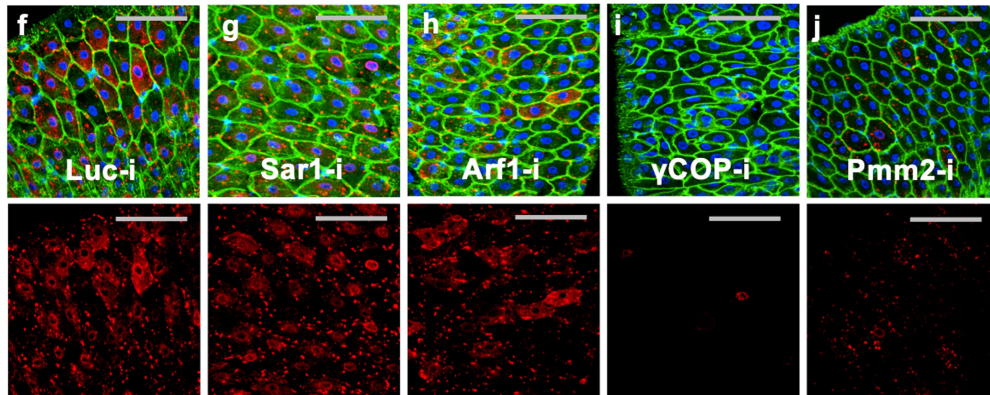
Extended Data Fig. 4 | See next page for caption.

Article

Extended Data Fig. 4 | Related to Fig. 2. Analysis of the dependency of PXo bodies on other canonical organelles. a, EM of midgut frozen section with immunogold-labeled GFP-PXo (examples highlighted with arrowheads) expressed in progenitors. **b**, Midgut EM shows unlabeled PXo bodies mainly in ECs (examples highlighted with arrowheads). A progenitor cell, as circled out by dashed line, can be distinguished from ECs, based on its basal localization, high electron density, lack of microvilli, and lack of mitochondria ("mt") cristae. A magnified view of the squared region, as presented in (**b'**), shows a PXo body in the progenitor. **c**, Midgut EM distinguishes the membranous PXo bodies (highlighted with arrowhead) from lipid droplets ("LD"). **d,e**, EM shows PXo body fragmentation in midguts with ubiquitous *γCOP* knockdown for 7d.

f,g,h,i,j, HA staining of midguts expressing *PXo-HA* together with *Luc* RNAi, *Sar1* RNAi, *Arf1* RNAi, *γCOP* RNAi, or *Pmm2* RNAi in ECs for 7d. Lethal giant larvae (Lgl) marks cell border. **k,l,m,n,o,p**, EM showing PXo bodies in ECs expressing *Luc* RNAi, *Pink* RNAi, *Parkin* RNAi, *Lamp1* RNAi, or *Abca* RNAi for 7d, with PXo body size quantification in (**q**). $n = 110$ (Abca-i[1]) or 120 (other groups). P values from bottom to top: 1.00, 0.747, 0.0162, 1.00, 1.00. **r,s,t,u**, EM showing PXo bodies in ECs expressing *Luc* RNAi ($n = 70$), *Rab7* RNAi ($n = 60$), or *Rab11* RNAi (line #1: $n = 70$; line #2: $n = 80$) for 3d, with quantification in (**v**). P values from bottom to top: 1.00, 0.490, 1.00. Data are mean ± s.e.m.. P values are calculated from one-way ANOVA with Bonferroni's multiple comparison test. Scale bars, 1 μm (**a**,**b'**, **c**–**e**, **k**–**p**, **r**–**u**), 10 μm (**b**), 50 μm (**f**–**j**).
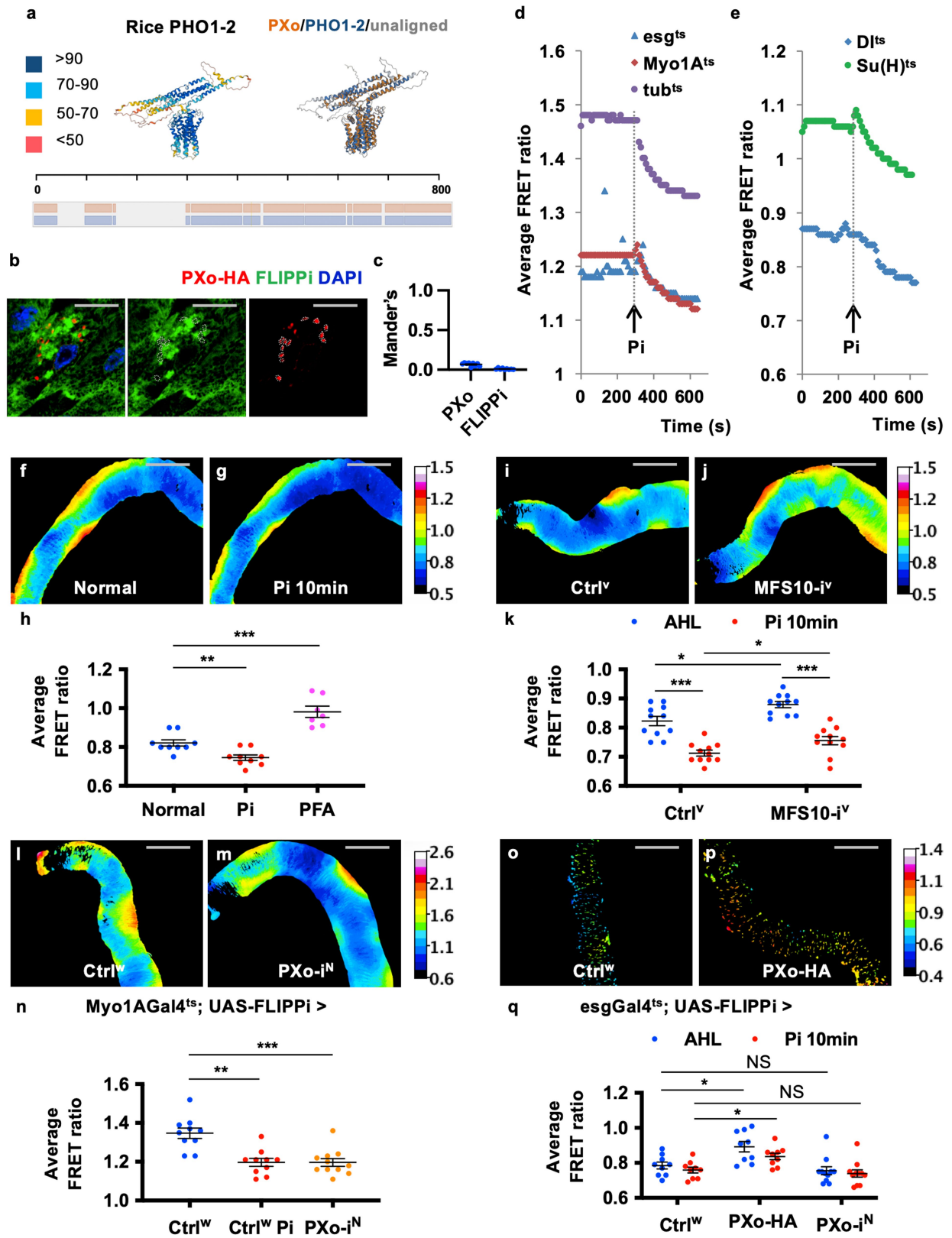
**Extended Data Fig. 5** | See next page for caption.

Article

Extended Data Fig. 5 | Related to Fig. 3. PXo structure and live imaging for cytosolic Pi. a, AlphaFold structure prediction of rice PHO1-2, with color-scaled visualization of the prediction confidence score. The pairwise structure alignment between PXo and PHO1-2 was shown on the right, with aligned regions superposed on one another and highlighted in color. The summary of amino acid sequence alignment was shown at the bottom, with aligned regions highlighted in color. **b**, A single Z-stack of confocal image of midguts expressing PXo-HA and FLIPPi together in the ECs for 7d. Separate channels of HA and YFP (FLIPPi) stainings are presented on the right of merged images. **c**, Co-localization analysis with the quantification of the PXo-FLIPPi and FLIPPi-PXo Mander's coefficients. $n = 9$ per group. **d**,**e**, Kinetics of the average FRET ratio (cpVenus/CFP) in the midguts expressing *FLIPPi* ubiquitously (*tub^{ts}*) or specifically in ECs (*Myo1A^{ts}*), progenitors (*esg^{ts}*), ISCs (*Dl^{ts}*) or EBs (*Su(H)^{ts}*) for 3–7 days. The imaging videos were captured for ~10 min. The time points adding an extra final concentration of 30 mM Pi (~300s, using sodium phosphate or potassium phosphate) to the AHL imaging buffer is indicated by black arrows. Note that a new steady cytosolic Pi level is reached ~5 min after the addition of extra Pi. **f**, Color-scaled visualization of FRET ratios in the posterior midgut with ubiquitous *FLIPPi* expression for 7d. The same area was imaged again 10 min after the addition of 30 mM Pi (**g**). **h**, FRET ratio quantification of midguts with ubiquitous *FLIPPi* expression for 7d on normal food before or after 30 mM Pi addition to the imaging buffer ($n = 9$), or with the last 4d on PFA food ($n = 7$). *P* values from bottom to top: 3.91E-3, 3.50E-4. **i**,**j**,**k**, FRET ratio visualization and quantification of ECs expressing *FLIPPi* alone or *FLIPPi* together with *MFS10* RNAi for 7d, before or 10 min after 30 mM Pi addition. $n = 11$ per group. *P* values from bottom to top: 9.77E-4, 9.77E-4, 0.0173, 0.0192. **l**,**m**,**n**, FRET ratio visualization and quantification of midguts expressing *FLIPPi* alone (by crossing to *Ctrl^{w}*, $n = 10$) or *FLIPPi* together with *PXo* RNAi (NIG line, $n = 11$) in ECs for 6d. *P* values from bottom to top: 1.95E-3, 4.03E-4. **o**,**p**, FRET ratios visualization of progenitors expressing *FLIPPi* alone or together with *PXo-HA* for 7d. **q**, FRET ratio quantification of midguts expressing *FLIPPi* alone ($n = 9$), *FLIPPi* together with *PXo-HA* ($n = 9$), or *FLIPPi* together with *PXo* RNAi (NIG line, $n = 11$) for 7d, before or after Pi addition. *P* values from bottom to top: 0.0210, 0.936, 0.0114, 0.778. Data are mean ± s.e.m. *P* values are from Wilcoxon signed rank test for same sample comparison before and after Pi addition in (**h**,**k**,**n**), two-tailed Mann-Whitney u test between different samples (**h**,**k**,**n**) or one-way ANOVA with Bonferroni's multiple comparison test (**q**). Scale bars, 10 μm (**b**), 200 μm (**f**,**g**,**i**,**j**,**l**,**m**,**o**,**p**).
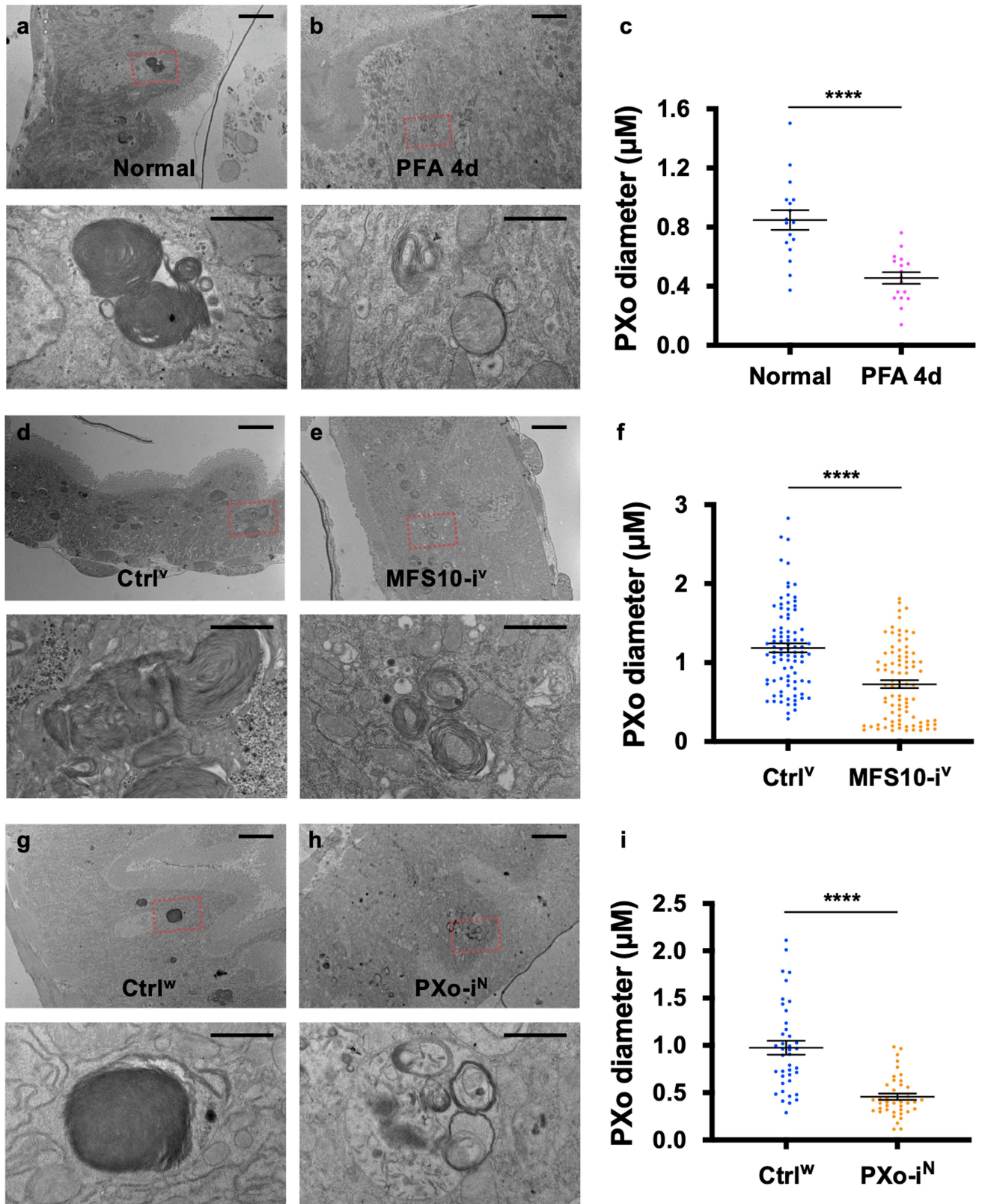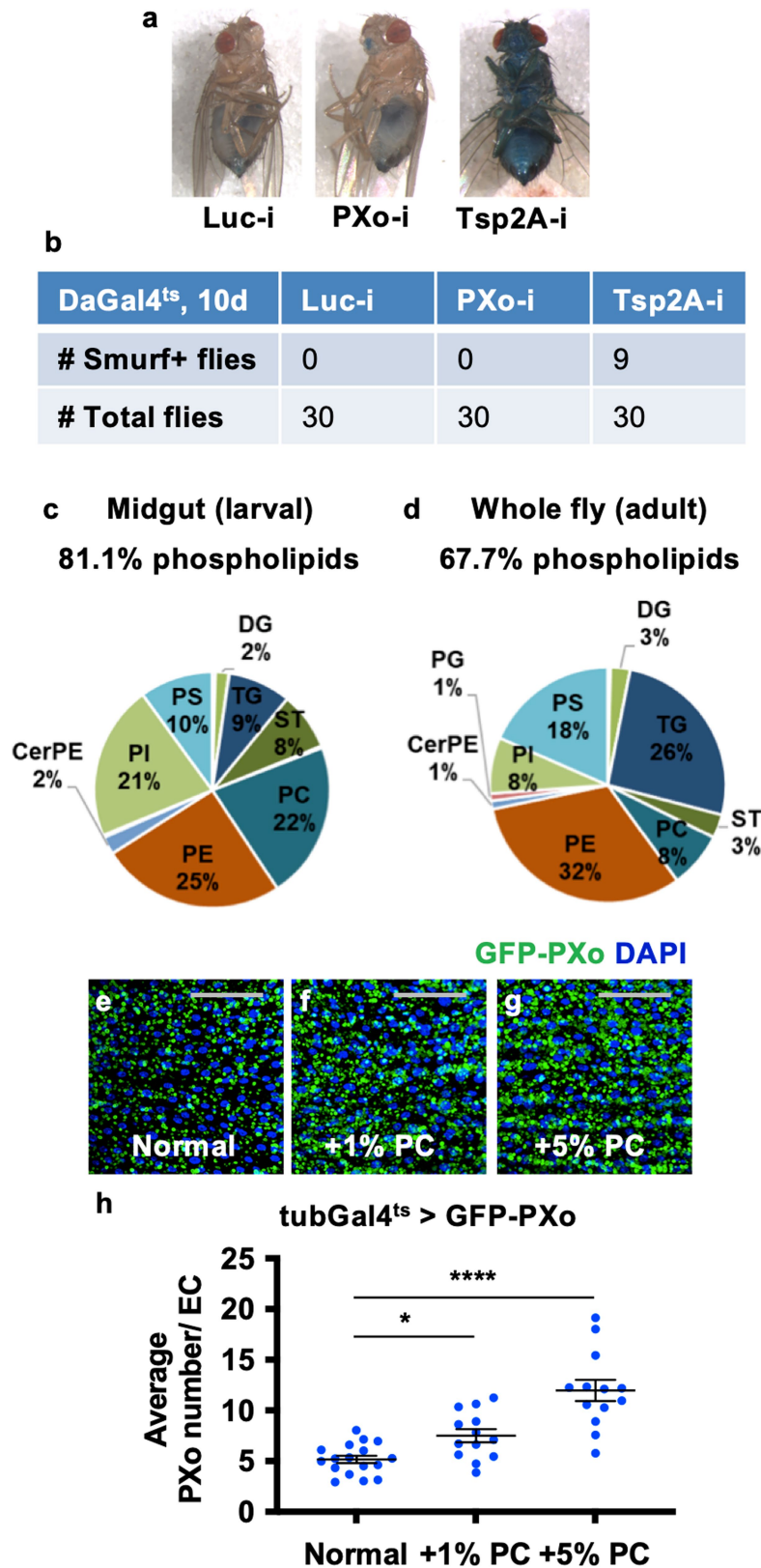
Extended Data Fig. 6 | Related to Fig. 4. EM analysis for the dependency of PXo bodies on Pi availability and PXo expression. a,b, EM of wild type (genotype: *Ore^R*) midguts with or without PFA feeding for 4d, along with magnified views of highlighted regions in the bottom and PXo body size quantification in (**c**). $n = 17$ PXo bodies were analyzed per group. $P = 1.28\text{E-}5$. **d,e**, EM of midguts with or without ubiquitous *MFS10* RNAi expression for 5d, along with a magnified view of highlighted regions in the bottom and PXo body size quantification in (**f**). $n = 91$ (*Ctrl^v*), 89 (*MFS10-i^v*). $P = 1.38\text{E-}8$. **g,h**, EM of midguts with or without ubiquitous *PXo* RNAi (NIG line) expression for 5d, along with magnified views of highlighted regions in the bottom and PXo body size quantification in (**i**). $n = 40$ PXo bodies per group. $P = 1.30\text{E-}9$. Data are mean ± s.e.m. *P* values are from two-tailed Mann-Whitney u test (**c,f,i**). Scale bars, 4 µm (**a,b,d,e,g,h,** top images), 1 µm (**a,b,d,e,g,h,** bottom images).

Article
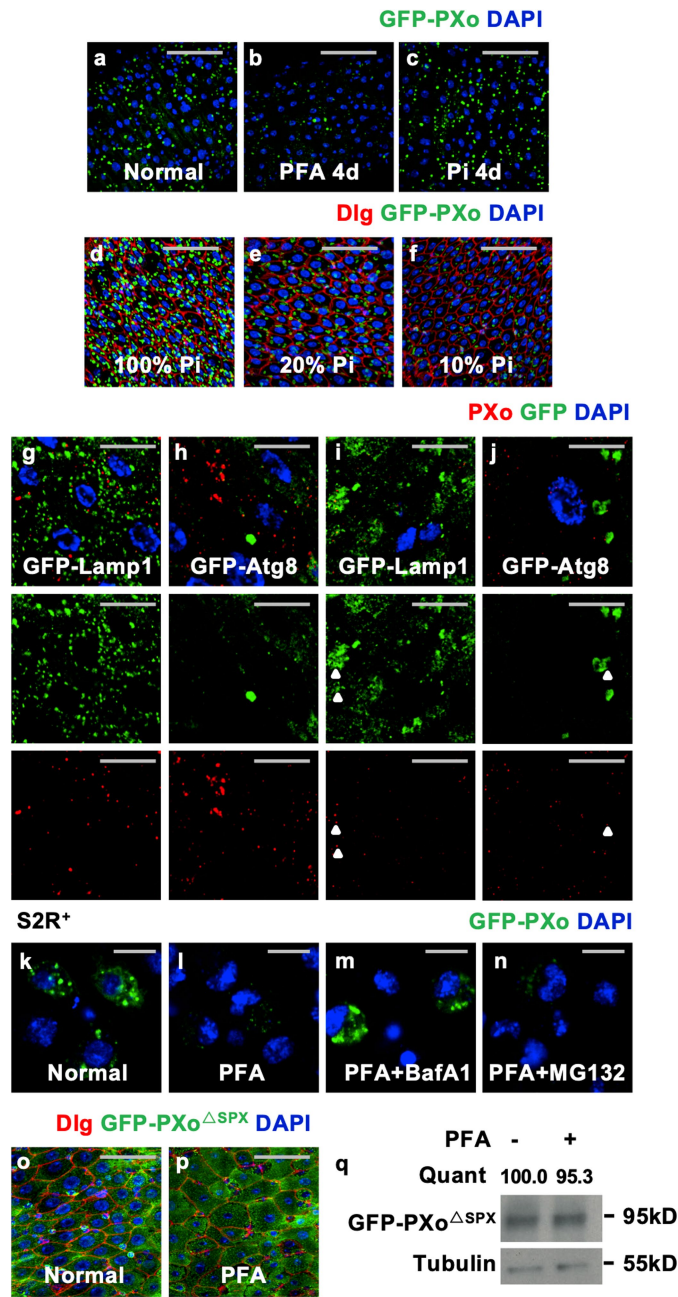
Extended Data Fig. 7 | Related to Fig. 4. Mechanistic analysis of Pi-sensitivity for PXo and PXo bodies. a,**b**,**c**, Midguts with *GFP-PXo* expression in ECs (driven by *Myo1AGal4*), with the last 4d on normal, PFA, or Pi food before dissection. **d**, **e**,**f**, Midguts with ubiquitous *GFP-PXo* expression for 7d, with the last 4d on CDF containing standard (100%), 20%, or 10% Pi. The staining for junctional protein Discs large (Dlg) marks cell borders. **g**,**h**,**i**,**j**, Anti-PXo staining of midguts with ubiquitous expression of *GFP-Lamp1* or *GFP-Atg8* (autophagosome marker) under normal feeding (**g**,**h**) or 4d PFA feeding conditions (**i**,**j**). A single Z-stack of confocal image is presented. Separate green and red channels are presented below merged images. Arrowheads highlight examples of co-localization. **k**,**l**, **m**,**n**, S2R^{+} cells expressing *GFP-PXo* with or without 24 hrs treatment of PFA, PFA together with BafA1, or PFA together with MG132. **o**,**p**, Midguts ubiquitously expressing *GFP-PXo*$^{\triangle SPX}$ for 7d, with the last 4d on normal or PFA food, were stained for GFP and Dlg. **q**, Immunoblot of midgut lysates with ubiquitous expression of *GFP-PXo*$^{\triangle SPX}$ for 7d, with or without the last 4d on PFA. Tubulin was the loading control. Quantification of relative normalized anti-GFP IB intensity is presented. Gel source data in Supplementary Fig. 1f. Scale bars, 50 μm (**a**–**f**, **o**,**p**), 10 μm (**g**–**n**).

a

Luc-i PXo-i Tsp2A-i

b

DaGal4ts, 10d	Luc-i	PXo-i	Tsp2A-i
# Smurf+ flies	0	0	9
# Total flies	30	30	30

c **Midgut (larval)**
81.1% phospholipids

d **Whole fly (adult)**
67.7% phospholipids

GFP-PXo DAPI

e Normal **f** +1% PC **g** +5% PC

h tubGal4ts > GFP-PXo

Average PXo number/ EC

Normal +1% PC +5% PC

Extended Data Fig. 8 | Related to Fig. 5. Further examination of PXo's relevance to intestinal barrier integrity or lipid metabolism. a,b, Smurf assay to evaluate the barrier function of midguts expressing *Luc* RNAi, *PXo* RNAi ubiquitously for 10 days. Prolonged *Tsp2A* RNAi expression was used as a positive control. **c,d**, Representation of different lipid categories in the previously characterized lipidomes of *Drosophila* larval midguts or adult whole bodies. **e,f,g,h**, GFP staining and PXo density quantification of midguts with ubiquitous *GFP-PXo* expression for 7d, with the last 3d on normal food ($n = 17$), or food containing additional 1% ($n = 13$, $P = 0.0393$) or 5% PC ($n = 13$, $P = 3.40E-8$). Data are mean ± s.e.m. *P* values are from one-way ANOVA with Bonferroni's multiple comparison test. Scale bars, 50 µm.
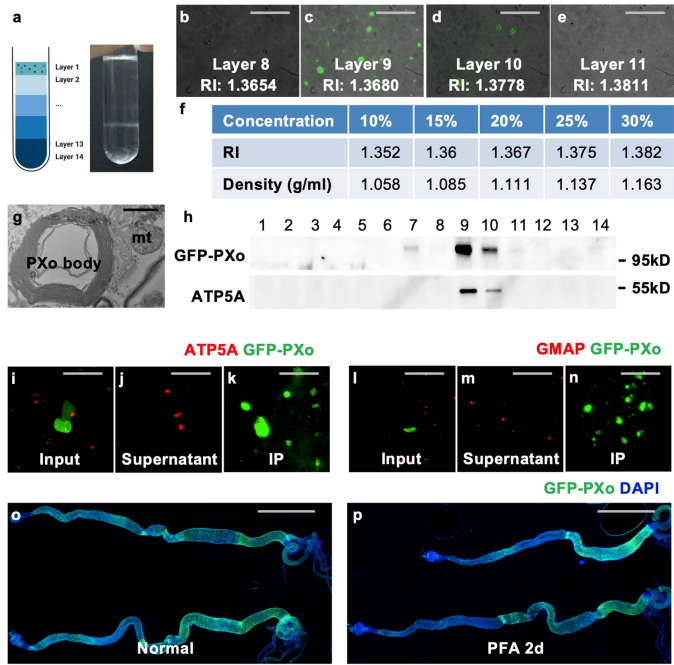
Extended Data Fig. 9 | Related to Fig. 5. PXo body extraction and purification methods. a, A centrifugation tube with midgut lysate OptiPrep gradient after ultracentrifugation, alongside with the cartoon created from BioRender.com depicting 14 gradient layers (fractions). **b,c,d,e**, Merged bright field and GFP fluorescent images of microscopic slides prepared from 15 μl aliquots of separated Layers 8–11. The refraction index (RI) for each Layer is also measured. **f**, RI measurement of 10%–30% serial concentrations of OptiPrep solutions, along with their calculated density. **g**, EM of a dissociated PXo body alongside a mitochondria (mt) from combined Layers 9-10. **h**, IB of the same volume of lysates from 14 separate Layers for GFP-PXo and ATP5A. Gel source data in Supplementary Fig. 1g. **i,j,k,l,m,n**, ATP5A and GMAP staining of midgut homogenate before (Input) and after immunoprecipitation (IP) of nanobody-conjugated Chromotek-GFP-Trap agarose beads, along with the flowthrough (Supernatant). **o,p**, Whole midguts with ubiquitous GFP-PXo expression for 5d, with the last 2d on normal food or PFA food. Scale bars, 50 μm (**b,c,d,e**), 1 μm (**g**), 10 μm (**i,j,k,l,m,n**), 1 mm (**o,p**).
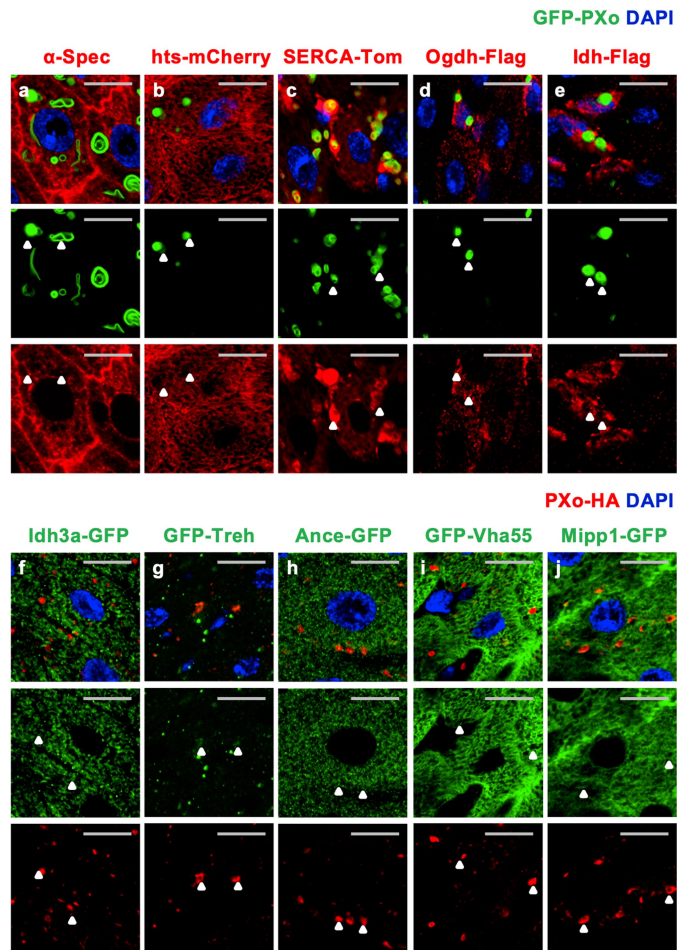
Extended Data Fig. 10 | Related to Fig. 5. Validation of identified PXo body proteins. a, α-Spec staining of midguts with ubiquitous expression of GFP-PXo. A single Z-stack of confocal image is presented, with separate green and red channels presented below merged images and white arrowheads highlighting examples of co-localization. **b,c,d,e**, Co-staining of GFP-PXo with hts-mCherry, SERCA-Tomato, Ogdh-Flag, or Idh-Flag ubiquitously expressed in the midgut. A single Z-stack of confocal image is presented, with separate green and red channels presented below merged images and white arrowheads highlighting examples of co-localization. **f,g,h**, Co-staining of EC-expressed PXo-HA with Idh3a-GFP expressed in a fosmid (**f**), or endogenously tagged GFP-Treh (**g**) or Ance-GFP (**h**). A single Z-stack of confocal image is presented, with separate green and red channels presented below merged images and white arrowheads highlighting examples of co-localization. **i,j**, Co-staining of PXo-HA and GFP-Vha55 or Mipp1-GFP expressed in ECs. A single Z-stack of confocal image is presented, with separate green and red channels presented below merged images and white arrowheads highlighting examples of co-localization. Scale bars, 10 μm.
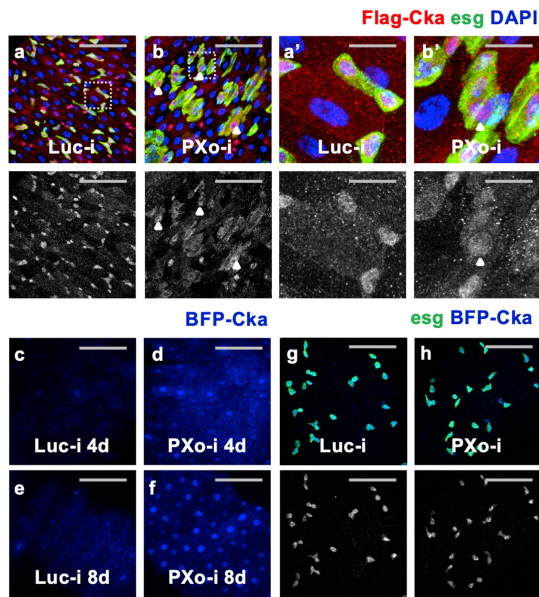
Extended Data Fig. 11 | Related to Fig. 6. Comparison of how PXo affects Cka expression in ECs and in progenitors. a,b, Flag-Cka staining of midguts expressing *Luc* RNAi or *PXo* RNAi in progenitors for 9d. A magnified view of regions highlighted with white dashed squares is presented in (**a′,b′**). The red channel images of anti-Flag staining are in grayscale below the merged images. White arrowheads highlight examples of progenitors that are differentiating towards ECs, as judged by their extended morphology, and enlarged nuclei size (**b,b′**). **c,d,e,f**, Midguts expressing *BFP-Cka* together with *Luc* RNAi or *PXo* RNAi in ECs for 4d or 8d. **g,h**, Midguts expressing *BFP-Cka* together with *Luc* RNAi or *PXo* RNAi in progenitors for 5d. The single-channel images of BFP-Cka fluorescence are presented in grayscale below merged images. Scale bars, 50 μm (**a,b,c,d,e,f,g,h**), 10 μm (**a′,b′**).
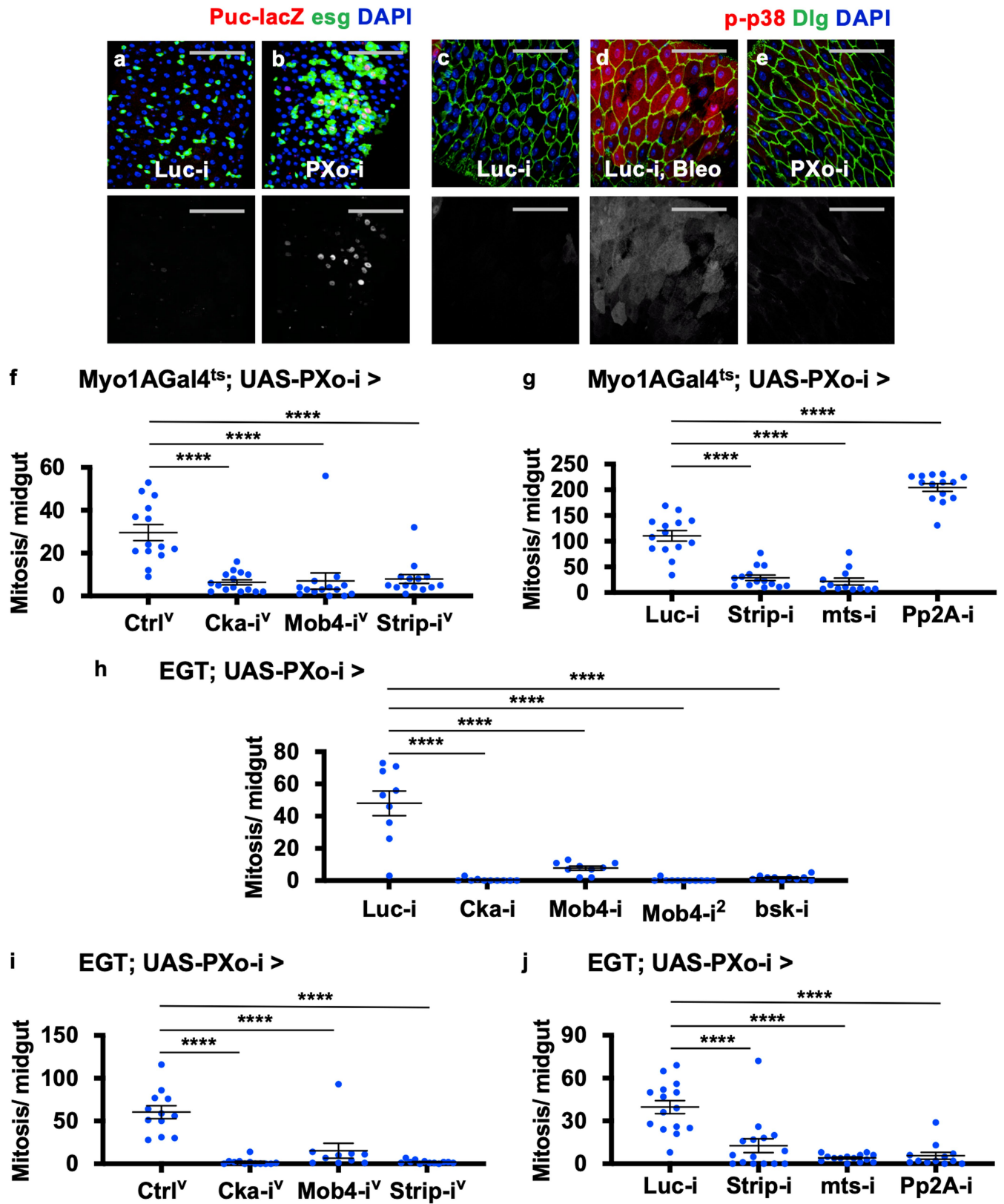
Extended Data Fig. 12 | See next page for caption.

Article

nature portfolio

Corresponding author(s):	Norbert Perrimon, Chiwei Xu
Last updated by author(s):	03/08/2023

Reporting Summary

Nature Portfolio wishes to improve the reproducibility of the work that we publish. This form provides structure for consistency and transparency in reporting. For further information on Nature Portfolio policies, see our Editorial Policies and the Editorial Policy Checklist.

Statistics

For all statistical analyses, confirm that the following items are present in the figure legend, table legend, main text, or Methods section.

n/a	Confirmed	
☐	☒	The exact sample size (*n*) for each experimental group/condition, given as a discrete number and unit of measurement
☐	☒	A statement on whether measurements were taken from distinct samples or whether the same sample was measured repeatedly
☐	☒	The statistical test(s) used AND whether they are one- or two-sided *Only common tests should be described solely by name; describe more complex techniques in the Methods section.*
☒	☐	A description of all covariates tested
☐	☒	A description of any assumptions or corrections, such as tests of normality and adjustment for multiple comparisons
☐	☒	A full description of the statistical parameters including central tendency (e.g. means) or other basic estimates (e.g. regression coefficient) AND variation (e.g. standard deviation) or associated estimates of uncertainty (e.g. confidence intervals)
☐	☒	For null hypothesis testing, the test statistic (e.g. *F*, *t*, *r*) with confidence intervals, effect sizes, degrees of freedom and *P* value noted *Give P values as exact values whenever suitable.*
☒	☐	For Bayesian analysis, information on the choice of priors and Markov chain Monte Carlo settings
☒	☐	For hierarchical and complex designs, identification of the appropriate level for tests and full reporting of outcomes
☒	☐	Estimates of effect sizes (e.g. Cohen's *d*, Pearson's *r*), indicating how they were calculated

Our web collection on statistics for biologists contains articles on many of the points above.

Software and code

Policy information about availability of computer code

Data collection	CFX Maestro Software for Bio-Rad CFX Real-Time PCR Systems
Data analysis	Imaris (x64 version 9.5.1) GraphPad Prism software version 9.4.0 R studio version 1.1.463 NIH Fiji Office 365 (Microsoft) AlphaFold (http://alphafold.ebi.ac.uk) RCSB PDB protein data bank server (http://www.rcsb.org/alignment) Proteome Software (https://proteomesoftware.com/) DAVID (https://david.ncifcrf.gov/) DIOPT Ortholog Finder (https://www.flyrnai.org/cgi-bin/DRSC_orthologs.pl) MSConvertGUI (https://proteowizard.sourceforge.io/) R package enviPick (https://rdrr.io/cran/enviPick/) Complex Enrichment Analysis Tool (COMPLEAT, https://flyrnai.org/compleat/) Molecular Interaction Search Tool (MIST, https://fgrtools.hms.harvard.edu/MIST/) Custom codes available at: http://github.com/charles-xu-ru/image-analysis

For manuscripts utilizing custom algorithms or software that are central to the research but not yet described in published literature, software must be made available to editors and reviewers. We strongly encourage code deposition in a community repository (e.g. GitHub). See the Nature Portfolio guidelines for submitting code & software for further information.

Data

Policy information about availability of data

All manuscripts must include a data availability statement. This statement should provide the following information, where applicable:

- Accession codes, unique identifiers, or web links for publicly available datasets
- A description of any restrictions on data availability
- For clinical datasets or third party data, please ensure that the statement adheres to our policy

> All data supporting the findings of this study are available within the Article and its Supplementary Information.

Human research participants

Policy information about studies involving human research participants and Sex and Gender in Research.

Reporting on sex and gender	not applicable
Population characteristics	not applicable
Recruitment	not applicable
Ethics oversight	not applicable

Note that full information on the approval of the study protocol must also be provided in the manuscript.

Field-specific reporting

Please select the one below that is the best fit for your research. If you are not sure, read the appropriate sections before making your selection.

☒ Life sciences   ☐ Behavioural & social sciences   ☐ Ecological, evolutionary & environmental sciences

For a reference copy of the document with all sections, see nature.com/documents/nr-reporting-summary-flat.pdf

Life sciences study design

All studies must disclose on these points even when the disclosure is negative.

Sample size	Sample sizes for midgut mitosis quantification were chosen empirically and based on the standards of the field. Example of a recent study: https://www.embopress.org/doi/full/10.15252/embj.2022110834. For quantification of shortest distance and electron micrographs, we analyzed a higher number of PXo bodies/graphs per condition because of higher variability. No sample size calculation was performed. The exact sample sizes are listed in the figure legends.
Data exclusions	This study involves no data exclusions. For mitosis quantification of the whole midgut, we would not count a midgut in rare cases when the gut is damaged during dissection or staining.
Replication	All experiments were reliably reproduced at least twice independently. Key findings (qRT-PCR, western blots, imaging) were reproduced 3 times (unless noted to be more than 3 times).
Randomization	A fixed number per tube of fly progenies of the desired genotypes were randomly selected and collected from each genetic cross for analysis.
Blinding	Our experiments did not include subjective measurements and therefore did not require blinding. pH3 staining exhibit a binary positive or negative pattern that is apparent for mitosis counting. Figure/movie quantifications were performed using automatic counting in NIH Fiji (imageJ) or Imaris.

Reporting for specific materials, systems and methods

We require information from authors about some types of materials, experimental systems and methods used in many studies. Here, indicate whether each material, system or method listed is relevant to your study. If you are not sure if a list item applies to your research, read the appropriate section before selecting a response.

Materials & experimental systems

n/a	Involved in the study
☐	☒ Antibodies
☐	☒ Eukaryotic cell lines
☒	☐ Palaeontology and archaeology
☒	☐ Animals and other organisms
☒	☐ Clinical data
☒	☐ Dual use research of concern

Methods

n/a	Involved in the study
☒	☐ ChIP-seq
☒	☐ Flow cytometry
☒	☐ MRI-based neuroimaging

Antibodies

Antibodies used	rabbit anti-pH3 (Millipore #06-570), mouse anti-GFP (Invitrogen A11120), rabbit anti-GFP (Invitrogen A6455), rabbit anti-RFP (Life Technologies R10367), rabbit anti-β-galactosidase (Cappel #0855976), rabbit anti-Pdm1 (from Xiaohang Yang), mouse anti-Pros (DSHB #MR1A; 1:50), mouse anti-HA (BioLegend #901514), mouse anti-HA (Thermo Scientific A-21287), rat anti-HA (Sigma-Aldrich 3F10), rabbit anti-PXo (this study), rabbit anti-cleaved caspase3 (Cell Signaling 9661S), goat anti-GMAP (DSHB #GMAP), mouse anti-Cnx99A (DSHB #Cnx99A 6-2-1), rabbit anti-Lgl (Santa Cruz sc-98260), mouse anti-ATP5A (Abcam ab14748), mouse anti-Hrs (DSHB #Hrs), mouse anti-Rab7 (DSHB #Rab7), rabbit anti-Lamp1 (Abcam ab30687), mouse anti-Dlg (DSHB #4F3), mouse anti-α-Spec (DSHB #3A9), rabbit anti-mCherry (Takara #632496), rabbit anti-Flag (Sigma-Aldrich F7425), rabbit anti-phospho-p38 MAPK (Cell Signaling #9211), mouse anti-Flag (Sigma F3040), rabbit anti-GAPDH (GeneTex GTX100118), mouse anti-Tubulin (Sigma T5168), Chromotek-GFP-Trap (Bulldog Biotechnology gta-20), rabbit anti-GFP (Abcam #6556).
Validation	The anti-PXo antibody generated in this study was validated by immunoblots and immuofluorescent staining as part of experimental design: the immunoblot with anti-PXo can successfully detect GFP-PXo over-expressed in S2R+ cells (Extended Data Fig. 2e); the immunostaining with anti-PXo unveils the same endogenous PXo expression pattern as the HA staining for PXo-2xHA knockin flies (Extended Data Fig. 2h, h'), whereas anti-PXo staining is diminished following PXo knockdown (Extended Data Fig. 2f, g). rabbit anti-Pdm1 from Xiaohang Yang is widely used as a marker for ECs in the fly midgut and exhibits a distinct staining pattern in the nuclei of ECs (example paper: Choi et al., 2011, PMID: 22049341). The validation for other commercial antibodies are listed on the product page of their purchase websites and the relevant literature documenting their success for the same applications in Drosophila could be found on BenchSci (https://app.benchsci.com/).

Eukaryotic cell lines

Policy information about cell lines and Sex and Gender in Research

Cell line source(s)	S2R+ cells were originally from Dr. Schneider and have been passaging in Perrimon lab and DRSC at Harvard Medical School for decades.
Authentication	The S2R+ cell line was obtained from the Drosophila RNAi Screening Center/Transgenic RNAi Project Functional Genomics Resources and Drosophila Research & Screening Center-Biomedical Technology Research Resource at Harvard Medical School. It has distinct morphology that can be relied on for quality control in routine passages. Moreover, it has been molecularly validated by transposable elements DNA sequencing (https://doi.org/10.1093/g3journal/jkab403).
Mycoplasma contamination	Contamination with mycoplasma is not an issue for Drosophila cultured cells. We regularly monitored the cultures for contamination by bacteria or fungus, and did not observe any signs of microbial contamination in cultures used in this study.
Commonly misidentified lines (See ICLAC register)	None.